Eindhoven University of Technology

MASTER

Exploring electrodeposition as a versatile method to synthesize porous electrodes for redox flow batteries

van Beek, Y.

Award date:
2021

Master thesis

Exploring electrodeposition as a versatile method to synthesize porous electrodes for redox flow batteries

Yvette van Beek

Department of Chemical Engineering and Chemistry

Eindhoven University of Technology

Committee Members:

Dr. A. Forner-Cuenca

MSc. R. R. Jacquemond

Prof. Dr. Ir. D.C. Nijmeijer

Dr. M.C. Costa Figueiredo

August 17th , 2020

Summary

Large-scale energy storage is needed to decarbonize our energy economy. Among many technological options, redox flow batteries are an attractive technology due to their ability to decouple power and energy, increased safety, and their potential to scale-up easily. However, current elevated capital costs limit the technology from widespread adaptation. The current generation of these batteries is still weak, which results in efficiency losses (overpotentials). Increasing the power density is a powerful strategy to decrease the costs of redox flow batteries.

One component that critically impacts the performance of the flow batteries are the electrodes. Electrodes are porous, conductive materials that are responsible for distributing liquid electrolytes, providing surfaces for electrochemical reactions, and sustaining mechanical compression. State-of-the-art electrodes feature poor electrochemical kinetics towards important reactions (all-vanadium) and poor durability under elevated potentials. In this thesis, the use of electrodeposition and metals (Cu, Ni) and bimetallic alloys (Cu-Ni) is proposed for the first time as a versatile method to fabricate porous electrodes for redox flow batteries. In addition, preliminary research is conducted towards the fabrication of bimodal porous electrodes to increase the electrochemically active surface area and to decrease pressure drop. We have gained some insight in the fundamentals of creating a conformal deposit through pulsed electrodeposition. It is a easy method to reduce hydrogen evolution during Ni deposition and to use lower concentration electrodeposition solutions to obtain larger current efficiencies. In addition, nucleation overpotential is decreased for pulsed electrodeposition, resulting in island growth that is closer towards kinetic control and thus improving the conformality of the coating.

Altogether, the straightforward method of electrodeposition can be used as a competent method to reduce fabrication costs and improve the performance of redox flow batteries.

Acknowledgements

I would like to show my appreciation for my daily supervisor, Rémy Jacquemond, who has helped me when times get tough and provided me with advice not only in my experiments, data, and discussion, but also supported me to cope with failures. He always expressed his sincere gratitude when I managed to get back up and helped me to act professional throughout my journey of writing this thesis. Without his support, I would not have been able to realize what I present to you in this work. I really enjoyed our discussions and it provided me with new ideas to think of and it showed me a whole new level of doing research.

Also, I would like to express my appreciation for my faculty supervisor, Antoni Forner-Cuenca, who thought me the tools to write, reassess, and present data in a proper manner. His critical questions and high interest towards my project and progress motivated me a lot and helped me to regain my focus when I got overwhelmed by all the new theory I had to learn and understand while starting with this project. I much appreciate the time and effort he has given me through update meetings and provided me with creative as well as critical feedback on my work.

I would also like to show my gratitude towards my professor, Kitty Nijmeijer, who provided me with critical feedback during my midterm examination and showed me where my strengths and weaknesses were. I am very grateful to have been part of her group, MMP, and that I was awarded the opportunity to do my graduation project in the group of Kitty. I really enjoyed the atmosphere she has created in her group and the fun activities ranging from celebrating holidays and birthdays together as well as the opportunity to join a conference on membrane materials.

I would like to thank Marta Costa Figueiredo as well for taking the time to provide me with feedback during my midterm examination, and being part of my examination committee.

I would like to also express my gratitude towards my colleague students in MMP who supported me during this period and I want to thank them for the nice discussions we had on my topic as well as theirs. I really enjoyed our much needed coffee breaks and the fun activities we planned. I feel very lucky to have had them as my colleagues since they have thought me a lot about electrochemistry and we could share our experiences to learn more about each other and about ourselves.

Finally, I would like to acknowledge the support of my friends and family, especially my roommate who had to put up with me while also working on her own thesis. They kept me

going when things got tough and it would not have been possible to present this work without their support and input.

Table of contents

Chapter 1 - Introduction

1.1 Towards a sustainable energy future – need for large energy storage

The world energy consumption has rapidly increased over the past century and is ever-growing due to population growth and industrialization [1], [2]. It is predicted to increase by 50% between 2018 and 2050 and will reach a yearly demand of 2.67×10^{14} kWh in 2050 [3]. To put this number into perspective: in 2011 a study was conducted on the annual electric energy per year for European households. It was found that the annual average electricity consumption is somewhere between 2500 – 3000 kWh/year per household [4].

In a perfect grid system we no longer rely on carbon based energy sources that are currently accountable for 25% of global greenhouse emissions [5]. Instead, we transition towards clean energy to preserve nature's resources and reduce pollution. Solar and wind energy are promising intermittent renewables that are already on the market and the costs of these renewables are declining. According to the International Renewable Energy Agency (IRENA), the electricity costs decreased between 2010 and 2019 with 28.6% in offshore wind, 38.4% in onshore wind, 82.0% in solar photovoltaics, and 47.4% in concentrating solar power [6]. In Lazard's Levelized Cost of Energy (LCOE) analysis of 2019, the electricity costs of wind (0.04 €/kWh), solar (0.04 €/kWh), coal (0.14 €/kWh), and gas (0.15 €/kWh) are presented [7]. A historical decline for renewables is supported by decreasing capital costs, improving technologies and increased competition between technologies, making them more interesting to employ. However, the power generation through intermittent renewables is not constant, which makes it difficult to provide supply when demanded (Figure 1). Additionally, electrical grids are only stable without energy storage when 10-20% of the energy generation originates from intermittent renewables [8]. This results in the need for storage technologies to create a smart grid system that complements the renewable standards.

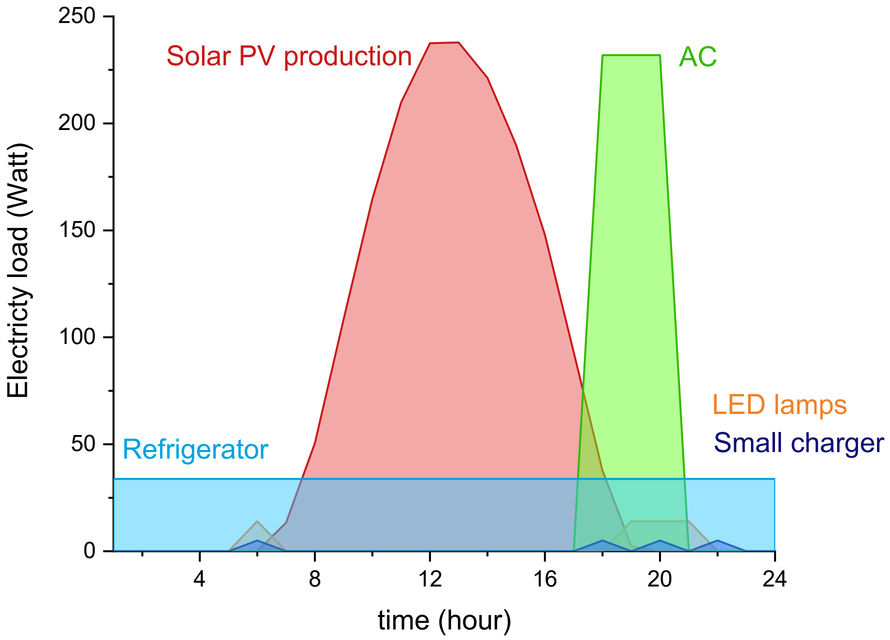

Figure 1 - The electricity load for solar energy production (red), refrigerator (light blue), LED lamps (orange), small charger (dark blue), and AC (green) are presented. Data adapted from the International Energy Agency (IEA) [9].

To tackle this challenge, grid-level energy storage technologies must be widely deployed to alleviate the intermittent supply of renewable sources. Currently deployed storage systems include pumped-hydro (that is currently responsible for >96% of the world storage capacity), compressed air energy storage (CAES), a variety of batteries, and flywheels and have a combined storage capacity of 170 GW. Pumped-hydro has low operation costs and a high durability and is therefore currently the most cost-effective storage system; however, the high capital costs and geographical constrains motivated researchers to investigate other technological solutions [10]. The technologies that are still in development include systems such as advanced lead-acid and flow batteries, superconducting magnetic energy storage, electrochemical capacitors, adiabatic CAES, hydrogen, and synthetic natural gas [11].

Among the available battery options, redox flow batteries (RFBs) have emerged as a promising technological alternative to store energy at a large scale given their ability to decouple energy and power, the projected low cost, and its location independence [12]–[14].

In the next section the redox flow battery fundamentals are presented. Many redox chemistries are being developed nowadays [12]–[14], but we decided to focus on all-vanadium redox flow batteries given their technological readiness level.

1.2 Redox flow batteries

RFBs (see Figure 2) are electrochemical devices that interconvert electrical energy and chemical energy through reduction and oxidation of electroactive species that are dissolve in liquid electrolytes. The liquid electrolytes, externally stored in tanks, are pumped through porous electrodes that provide the electrochemical active surface area (ECSA) for the redox reactions to take place. The electrodes are separated by an ion exchange membrane (IEM) that allows ion transport for electroneutrality and prevents crossover of the active species between both compartments.

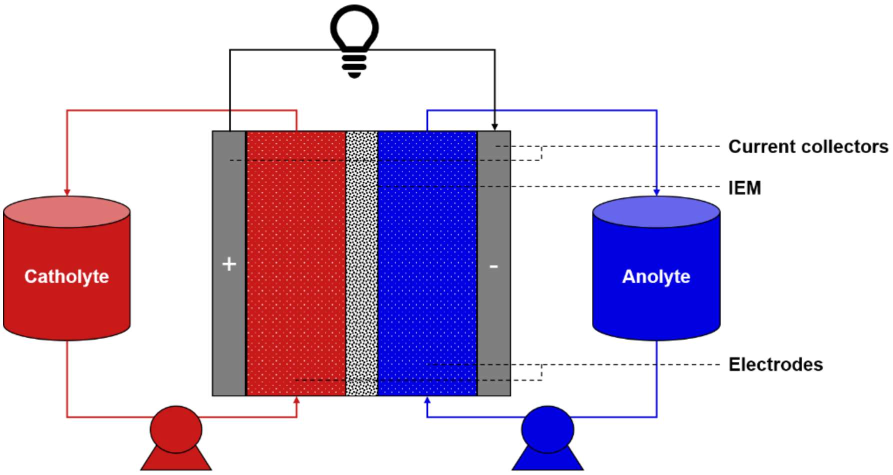

Figure 2 - A schematic representation of a redox flow battery that consists of a cell stack (current collectors, electrodes and ion exchange membrane) where ionic liquids (catholyte and anolyte) are stored in tanks and pumped through the system [12].

The operating voltage of the battery is determined by the chemical potentials of the electroactive species in both electrolytes. According to Kim et al, past studies have focused on redox species combinations to achieve higher efficiency, longer cycle live, and higher energy and power densities [15]. The typical OCVs of studied flow battery chemistries e.g. V/V, H/Br, Zn/Br, and Fe/V are 1.4 V, 1.1 V, 1.82 V, and 1.02 V, respectively [16]–[19]. However, the practical voltage of the system is usually found to be lower due to a low energy efficiency (EE) of the system.

In order to improve the EE of a redox flow battery, voltage losses due to polarization should be minimized. In Figure 3, three types of polarization losses are presented that are distinguished for redox flow batteries: kinetic polarization (activation losses), ohmic losses and mass transfer limitations. These losses (overpotentials) are subtracted from the open circuit voltage (OCV) and result in the cell potential (E_{cell}) of the RFB.

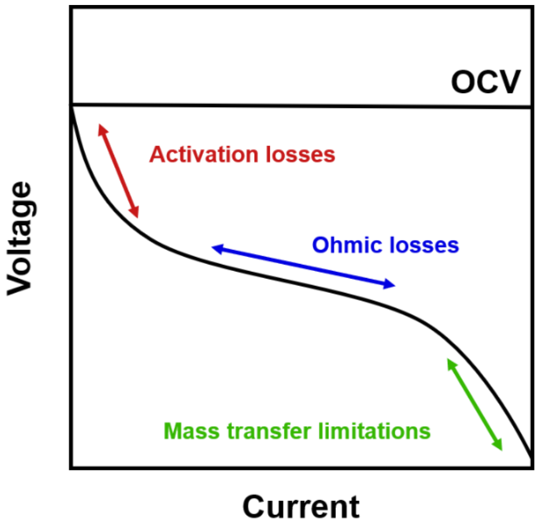

$$OCV - \eta_{act} - \eta_{ohm} - \eta_{mt} = E_{cell}$$

Figure 3 - The performances losses for a redox flow battery are presented in this polarization curve. The open circuit voltage (OCV) is shown, as well as the activation losses (red), ohmic losses (blue), and mass transfer limitations (green). The cell potential (E_{cell}) is the OCV minus the performances losses. Figure adapted from REF.

The origin of the different polarization losses are described as follows:

- The activation overpotential (η_{act}) arises at each electrode when energy is converted. The activation overpotential is related to electrochemical kinetics and can be described using the Butler-Volmer equation [20]. The cell current density is a function of the exchange current density (j_0), where a higher j_0 results in a lower η_{act}, and therefore improving the performance. At low current densities, the η_{act} are the main contributors to performance loss.
- In the mid current density range, ohmic losses (η_{ohm}) due to the resistive behavior of the IEM dominate.
- At higher current densities, mass transfer losses (η_{mt}) in the electrode diffusion layers dominate until the limiting current density of the cell is reached.

Polarization losses can be prevented by choosing redox species with fast kinetics and low viscosity, a highly ionically conductive electrolyte, highly electrical conductive current collectors, and a proper flow channel design. This results in a lower overpotential and higher energy densities are obtained for RFBs [21].

The reference redox system of state-of-the-art RFB systems is the all vanadium redox flow battery. We choose to focus our attention on this system, because it is the only chemistry that has been effectively commercialized [14]. In the case of vanadium redox flow batteries (VRFB), vanadium salts are dissolved in aqueous sulfuric acid. The redox species contain vanadium that has four adjacent oxidation states: V^{2+}/V^{3+} and VO^{2+}/VO_2^+. Figure 4 shows the redox reactions of each vanadium couple occur at the electrodes during charge and discharge.

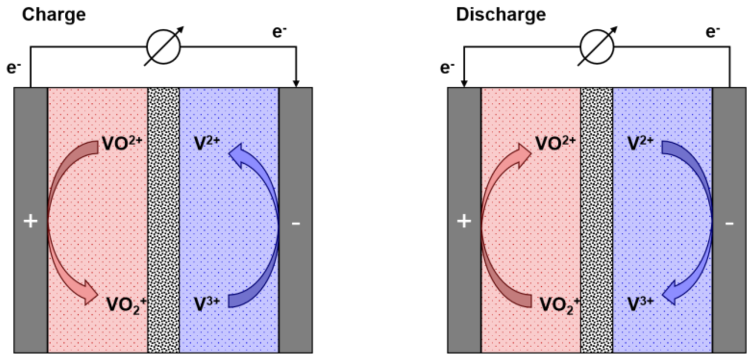

Figure 4 – Schematic representation of the charge and discharge cycle of vanadium species in a redox flow battery. During charge, oxidation occurs at the positive electrode and reduction at the negative electrode. For discharge the thermodynamic reactions occur: oxidation at the negative electrode and reduction at the positive electrode.

The half-cell reactions and the standard reduction potentials at both electrodes are described as [15]:

$$\text{Positive electrode: } VO_2^+ + 2H^+ + e^- \rightleftarrows VO^{2+} + H_2O \quad E^0 = 1.00\,V \tag{1}$$

$$\text{Negative electrode: } V^{2+} \rightleftarrows V^{3+} + e^- \quad E^0 = -0.26\,V \tag{2}$$

$$\text{Cell reaction: } VO_2^+ + 2H^+ + V^{2+} \rightleftarrows VO^{2+} + V^{3+} + H_2 \quad E_{cell} = 1.26\,V \tag{3}$$

Advantages of VRFBs is that cross-contamination is less invasive since vanadium is the active species in both the anolyte and catholyte. The cell capacity decreases due to cross-over and electrolyte decay, however it is easy to rebalance the electrolyte by pumping it in and out and therefore the lifespan of VRFB is prolonged [14]. However, the traditional sulfuric acid based

VRFBs are hindered due to the solubility and stability of the high concentration of vanadium species (>1.5 M) in the sulfuric electrolyte. The operational temperature window for state-of-the-art VRFBs is 10 to 40 °C, since outside of this temperature range the vanadium electrolytes form solid precipitates. This results in sluggish reactions kinetics and increases the activation overpotential. As a consequence, the electrochemical performance of the VRFB is limited by its low energy density and large activation overpotential, and this increases the costs of the VRFB [22], [23].

The electrode is a major component that leads to a large activation overpotential. The electrodes impact the kinetic, mass transfer, and ohmic overpotentials as well as playing a role in the durability of the battery. State-of-the-art electrode materials for VRFB include graphite felts that have a wide operating potential range in aqueous media, good chemical and mechanical stability, high electrical conductivity and are low cost materials [24]. However, in these aqueous conditions, the electrochemical activity of pristine carbon materials is quite poor for vanadium chemistry, due to the sluggish reaction rates of the vanadium species and due to improper wetting of the electrode material. Possible strategies to decrease the activation overpotentials of VRFB lead to the research on surface modifications and pretreatments to improve the electrode performance. A first approach is the fabrication of graphene oxide nanoplatelets (GONPs) that accommodate oxygen-containing functional groups on the surface. The functional groups provide catalytic sides for the vanadium redox species. Cyclic voltammetry measurements of the GONPs indicate an improved reversibility for both VO^{2+}/VO_2^{+} and V^{2+}/V^{3+} redox couples compared to pristine graphite; thus improving the performance of vanadium species reactions [25]. In line with the first approach, nitrogen-doped mesoporous carbon (N-MPC) is also demonstrated to result in enhanced performance for VRFB. It also facilitates the redox reactions of the vanadium species and therefore shows enhanced catalytic activity compared to undoped mesoporous carbon and graphite electrodes [26]. Another approach to modify the surface chemistry by increasing the oxygen content is a thermal pretreatment (thermal oxidation). It was found that this bulk pretreatment led to an improved oxygen content that again improves vanadium kinetics and also increases the wettability in aqueous media. However, charge-transfer resistance is increased due to an increased oxygen content and the ECSA decreases for higher pretreatment temperatures (due to partially burning of electrode fibers and binder). It is proposed that a high surface area and oxygen content facilitates both a reduction in charge-transfer and mass-transfer resistance [27], aiming for a more targeted method that is proposed to be more effective. The strategies mentioned before all focused on using functionalization techniques to increase the wettability and functional groups on the surface.

Another strategy that has been applied is decorating the surface with metallic particles. It appears to be a viable method to improve the catalytic activity of carbon electrodes. The fabrication of copper nanoparticles-deposited graphite felt electrodes showed improved kinetics for the V^{2+}/V^{3+} redox couple. Low concentrations of $CuSO_4$ (<10 mM) were added to the electrolyte and decorated the electrode in the negative electrolyte [28]. The use of copper nanoparticles is of interest, because it is a relatively abundant and could reduce the costs of VRFB. Improved performance was found for these decorated electrodes, however, there is not yet a clear fundamental understanding of the electrodeposition process, especially for 3D scaffolds.

In addition, a method to increase the ECSA to facilitate more redox reactions is the use of a different porous electrode material: metals. A better corrosion resistance, higher electrical conductivity, and better mechanical properties compared to carbon electrodes makes these metallic porous electrodes a material of interest [29]. Nickel (Ni) foams have been used in water splitting electrodes and proven to be efficient, scalable and recyclable [30].

The current field is lacking a systematic approach that enables tunable surface modification of porous electrodes for RFBs using well-controlled techniques. Importance lies in the fundamental understanding of structure-function relationships and ultimately fabricate a porous scaffold that may withstand the test of time by showing an improved durability and performance.

1.3 Scope of the research project

In this thesis, we explore the application of electrodeposition as a flexible methodology to fabricate porous electrodes for redox flow batteries with tailored functionalities. Utilizing the possibilities of electrodeposition, we employ this method to engineer porous electrodes by introducing copper and binary Ni-Cu alloy deposits onto carbon and metallic substrates to tackle two pressing challenges in state-of-the-art redox flow batteries (Figure 5):

1- ***Enhancing the electrocatalytic activity of porous carbon electrodes for all-vanadium redox flow batteries through the electrodeposition of copper.*** Redox reactions in all-vanadium redox flow batteries suffer from sluggish reaction rates which result in increased activation overpotentials and low system efficiency. Inspired by the work of L. Wei et al[28], we investigate the electrodeposition and application of copper particles on the carbon electrode to boost the V^{2+}/V^{3+} redox reactions. We are particularly interested in fundamentally understanding how to tune the electrodeposition process on two-dimensional, model electrode surfaces and the translation of these learnings onto porous, three-dimensional electrodes. The ultimate goal is to control the particle size, morphology, and coating morphology using this method.

2- ***Synthesizing porous electrodes with bimodal pore size distributions through electrodeposition of binary alloys and subsequently followed by de-alloying.*** Providing both a high ECSA to facilitate redox reactions and mass transfer requires complex microstructures with control at multiple length scales. Here, we explore the application of electrodeposition of nickel-copper alloys that is subsequently followed by electrochemically-assisted dealloying to form a hollow structure with a bimodal pore size distribution. We hypothesize that nickel scaffolds have the potential to improve stability of the porous electrode under high voltages, under which carbon materials are prone to degradation.

3- ***Paving the way for future work on electrodeposition for catalysis and material design.*** This thesis should be considered as the first step towards the development of electrodeposition as a versatile tool to tailor novel electrodes for RFBs.

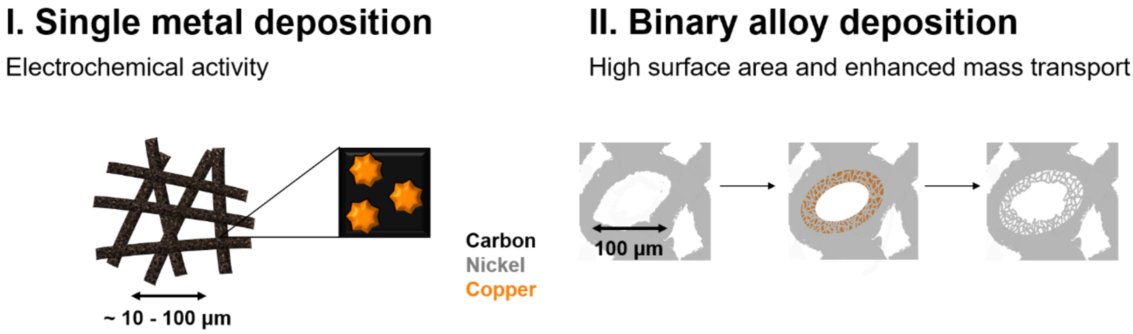

Figure 5 - Two novel approaches to fabricate porous electrodes for redox flow batteries are schematically shown. I. copper is electrodeposited onto porous carbon electrodes to enhance the electrocatalytic properties of the electrode. II. A Ni-Cu alloy is electrodeposited onto nickel foam and subsequently copper is dealloyed from the structure.

Chapter 2 - Experimental methods

Electrodeposition was used to coat Cu, Ni and NiCu alloy films on a variety of 2D and 3D substrates. Then, the prepared materials were characterized in terms of morphology, microstructure, and chemical composition. Finally, the electrochemical properties such as electrochemical surface area, transport properties and current efficiencies are determined for the fabricated materials. In order, the synthesis, physiochemical and electrochemical characterization are described.

2.1. Synthesis

2.1.1. Substrates

Ni foil (0.125 mm thick, purity ≥ 99.9%, Sigma-Aldrich) and graphite foil (0.254 mm thick, purity 99.8% (metals basis), Alfa Aesar) were used as 2D, flat substrates. Carbon electrodes (FuelCellStore) and Ni foam (NI003840 Nickel, 0.9 mm thick, purity 99.5%, porosity 93%, Good Fellow) were used as 3D scaffolds. In Table 1, the carbon electrodes materials and their properties are presented. In Figure 6, the morphology of the carbon electrodes are presented.

Table 1 - Properties of carbon electrodes. Adapted from [31].

Commercial name	Thickness* (mm)	Binder/Woven	Pore sizes* (µm)
Sigracet 39AA	0.32 ± 0.01	‘high content’ binder	63 (and 1-2 between graphite flakes)
Toray Paper	0.35 ± 0.01	‘low content’ binder	31
Freudenberg 23	0.21 ± 0.01	Hydroentangling process	22
ELAT Hydrophilic	0.38 ± 0.01	Woven	10-15 and 85 (bimodal)
AvCarb Felt	6.0 ± 0.1	Woven filament yarn	60

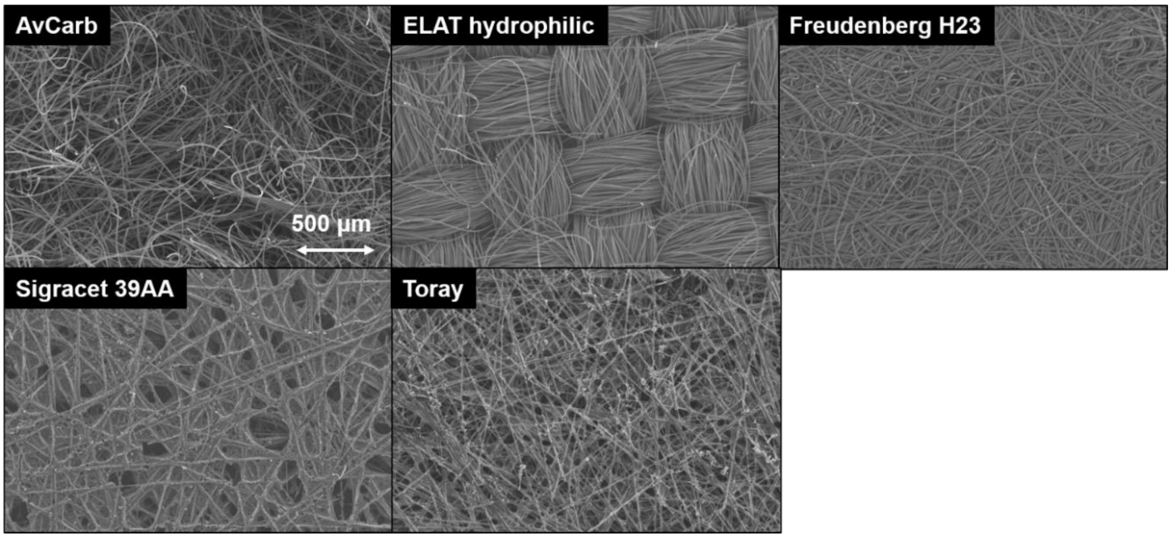

Figure 6 - The scanning electron microscope (SEM) images are presented of the different carbon electrode materials at a magnification of 50x.

2.1.1.1 Thermal pretreatment and cleaning procedure

The wettability of the electrodes was improved by introducing a thermal pretreatment to create oxygen groups on the surface, increasing the hydrophilicity. The carbon electrodes were first placed on an aluminum foil tray and heat treated in a box oven under an air atmosphere. The temperature was increased from 20 °C to 400 °C in three hours and was hold at 400 °C for twelve hours. The oven was cooled down by natural convection and the samples were retrieved when the oven was cooled down to RT.

Before deposition, the electrode is immersed in acetone (20 mL) for five minutes. Subsequently, it is immersed in ultrapure water (18.2 MΩ, 50 mL) for five minutes, put into 1 M H_2SO_4 solution (20 mL) for 10 minutes (20 mL), and ultrapure water (18.2 MΩ, 50 mL) for five minutes, in each step the electrode was stirred for ten seconds in solution and the electrode was dried in between the steps. After the cleaning steps, the electrode is dried in a vacuum oven overnight at 80 °C.

After deposition, the electrode was subsequently immersed in ultrapure water (18.2 MΩ, 50 mL), acetone (20 mL), ultrapure water (18.2 MΩ, 50 mL), and ultrapure water (18.2 MΩ, 50 mL). For all steps, the electrode is stirred for ten seconds and dried with tissue paper in between steps. The electrode is stored in a vial (20 mL) overnight and stirred every now and then. After 24 hours, the electrode is dried in a vacuum oven overnight at 80 °C.

2.1.2. Chemicals

In Table 2, all chemicals used are listed. Acetonitrile and ultrapure water were used as solvents for the electrodeposition. Tetraethylammonium tetrafluoroborate and sulfuric acid were used as electrolytes. Boric acid was added to Ni and NiCu solutions. Copper(II) sulfate and Nickel(II) sulfamate were used in aqueous electrodeposition solutions. Copper(II) tetrafluoroborate was used in acetonitrile electrodeposition solutions.

Table 2 - The chemical compound are listed with their formula, molecular weight, and supplier.

Chemical compound	**Formula**	**Molecular weight [g mol^{-1}]**	**Purity [%]**	**Supplier**
Acetonitrile	CH_3CN	41.05	99.9	Merck
Boric acid	H_3BO_3	61.83	99.97	Sigma-Aldrich
Copper(II) sulfate pentahydrate	$CuSO_4 \cdot 5H_2O$	249.69	98.0	Sigma-Aldrich
Copper(II) tetrafluoroborate (anhydrous)	Cu(II) BF_4	237.16	25.8[1]	Sigma-Aldrich
Nickel(II) sulfamate tetrahydrate	$Ni(H_2NSO_3)_2 \cdot 4H_2O$	322.93	98	Sigma-Aldrich
Sulfuric acid	H_2SO_4	98.08	95-98	Sigma-Aldrich
Tetraethylammonium tetrafluoroborate	$TEABF_4$	217.06	>98	TCI Europe

2.1.3. Electrodeposition of single metals

Electrodeposition was performed under ambient conditions in a three-electrode cell (see Figure 7a) with a platinum counter electrode (CE, large surface area ~5 cm^2) and an Ag/AgCl (3 M NaCl, EQUILABRIUM RRPEAGCL2-EQ low profile AgCl) reference electrode (Ref). The working electrode (WE) materials are mentioned for each experiment specifically. All potentials were reported versus the Ag/AgCl reference. Cyclic voltammetry was performed to determine the reduction potential for each experiment. The experiments performed were either direct current (dc) or direct potential, pulse current controlled, or reverse pulse current

---

[1] This is the copper content in Cu(II) BF_4.

controlled. Parameters that were changed during experiments are the applied current, applied voltage, total charge, and total time of the dc and pulsed experiments.

During this project, two set-ups were used. In Figure 7b, setup I is presented and it was fabricated by ourselves. The potentiostat was located in a lab without a fume hood. For safety reasons the electrodeposition of Cu, Ni, and NiCu alloy was performed in an enclosed system. The cap ensured an enclosed system during Ni and NiCu alloy electrodeposition.

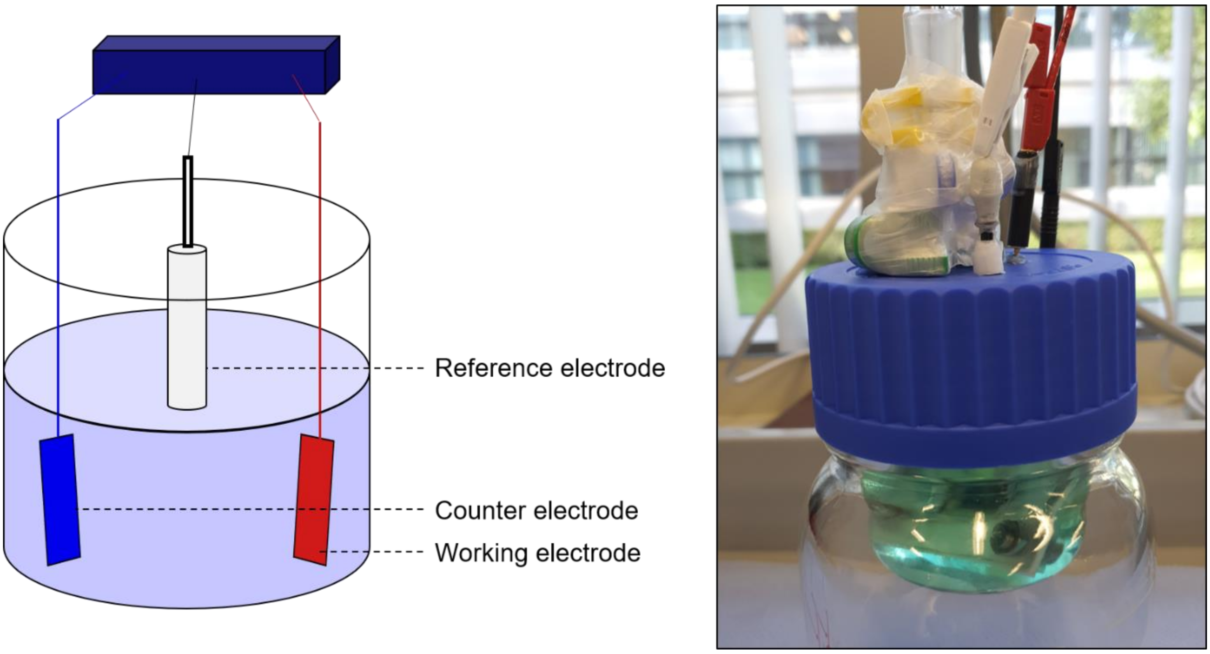

Figure 7 – a) A general schematic of a three electrode cell consisting of a working electrode (red), counter electrode (blue), and a reference electrode (white). b) The enclosed electrochemical cell fabricated by ourselves (setup I). A beaker without a beak was inserted into a flask with cap. The cap was modified to accommodate the three electrodes.

During the project, a new electrochemical cell was purchased (titration vessel from Metrohm, 50 - 150 mL) and used to replace the self-built cell. In Figure 8, setup II is presented.

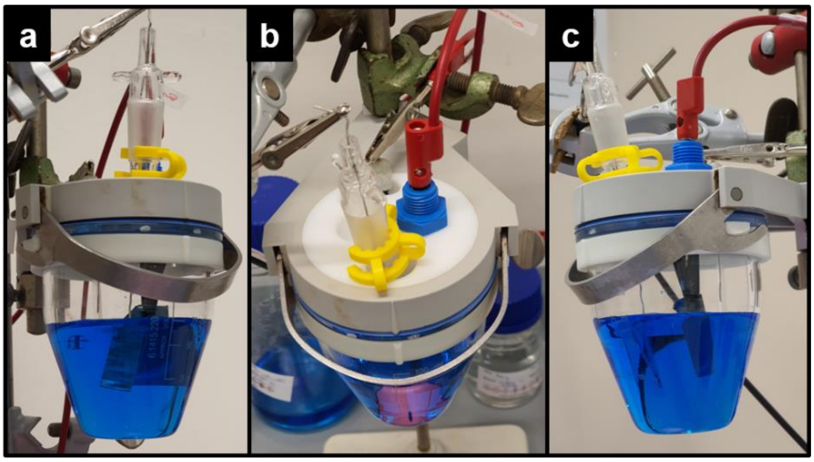

Figure 8 – Setup II containing an electrochemical cell. The left side (a), the top (b), and the right side (c) are shown. The CE is positioned facing the WE and the Ref is positioned close by the WE and further away from the CE (since the pH difference that might occur during electrodeposition).

To ensure a fixed electrode area (2.82 cm^2), the electrode was clamped between two squared frames, as presented in Figure 9. For the new cell the fabricated frame was too large and therefore new electrodes were cut into pieces of 0.5 × 1.5 cm^2. The electrodes were clamped and immersed at exactly 1.0 cm height in the electrolyte, resulting in an area of 1 cm^2 to be immersed into the deposition solution. This assured a fixed current density for all current controlled electrodeposition experiments. For each experiment, it is specified if the electrode was clamped or the frame was used.

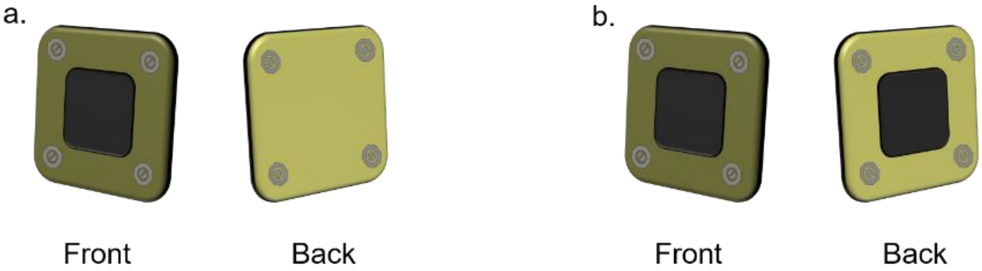

Figure 9 - A schematic representation of the frames used to hold the electrodes for electrodeposition. a) the frame is open on one side and closed on the other side. b) the frame is open on both sides. The inner area of the frame is 2.82 cm^2 for both frames.

2.1.3.1. Electrodeposition of copper onto carbon electrodes from aqueous solution

Copper was deposited from a solution containing 0.1 M $CuSO_4 \cdot 5\,H_2O$ in 0.5 M H_2SO_4 onto ELAT Hydrophilic. The frame with both sides open was used (Figure 9b) in setup I (Figure

7b). Copper crystals were deposited through potentiostatic and pulsed electrodeposition (PED). A on time (t_{on} = -0.3 V) was applied and followed by an off time (t_{off} = 0.0 V). Further parameters are specified in section 4.2.3.3..

Additionally, copper was deposited from a solution containing either 0.1 M or 1.25 M $CuSO_4$ in 0.5 M H_2SO_4 onto Freudenberg H23. The experiments were performed using setup II (Figure 8). A fixed area of 1 cm^2 was used. Current controlled PED was performed existing of a cathodic pulse (t_c), an anodic pulse (t_a), and an off time (t_{off}). Further parameters are specified in section 4.2.3.4..

2.1.3.2. Electrodeposition of copper from organic solvent

Copper was deposited from solution containing 0.1 M anhydrous copper(II) tetrafluoroborate and 0.1 M tetraethylammonium tetrafluoroborate in MeCN onto ELAT hydrophilic. The frame with both sides open was used (Figure 7b). Copper crystals were deposited at a constant reduction potential of -0.3 V and -0.85 V. Deposition times of 10, 20, 30, and 60 minutes were taken.

2.1.4. Electrodeposition of nickel

PED was used to electrodeposit nickel onto graphite foil (A = 1 cm^2) from 350 g L^{-1} $Ni(H_2NSO_3)_2$ and 25 g L^{-1} H_3BO_3 using the setup mentioned in Figure 8. Fixed current densities of -35 mA cm^{-2}, +35 mA cm^{-2} and 0 mA cm^{-2} were subsequently applied for 500 cycles as cathodic pulse (t_c = 0.05, 0.1, 0.5, and 1 s) , anodic pulse (t_a = 2 ms) and off time (t_{off} = 1 s), respectively.

2.1.4. Electrodeposition of alloys

NiCu alloy films were deposited from solution containing 0.8 M $CuSO_4 \cdot 5H_2O$ and 0.05 M $Ni(H_2NSO_3)_2 \cdot 4H_2O$ with 0.4 M H_3BO_3 in an enclosed system due to the toxic nature of nickel salts. Films were deposited onto Ni foil and graphite foil as substrates. The frame with one side open and one side closed was used (Figure 9a). NiCu alloy films were deposition at constant potential ranging between -0.70 to -1.15 V. The deposition charge limit is fixed at 8 C per 2.82 cm^2.

2.2 Characterization

2.2.1 Morphology

Imaging of the surface was done using a scanning electron microscope (SEM, JEOL). Two different settings were used: 1) The secondary electron detector (SED) was used at 15.0 keV with a WD of 10 mm, a P.C. of 50, and magnifications of 500x, 2,500x and 5,000x at three different spots in the sample. If there was a lot of deviation between the imaged parts, another measurement was performed to increase measurement statistics. 2) The SED was used at 20.0 keV with a WD of 10 mm, a P.C. of 35, and magnifications of 50x, 500x, 2,000x, and 10,000x.

The imagining of the bulk of Cu onto Ni foil was done using a focused ion beam SEM (FIB-SEM). The samples was etched away to exposed internal surfaces with an Ga^+ ion beam as depicted in Figure 10. The settings were 10.0 keV with WD of 10.1 mm, a current of 93.3 pA, and a magnification of 12,000 x. The incidence angle was 51.0 °.

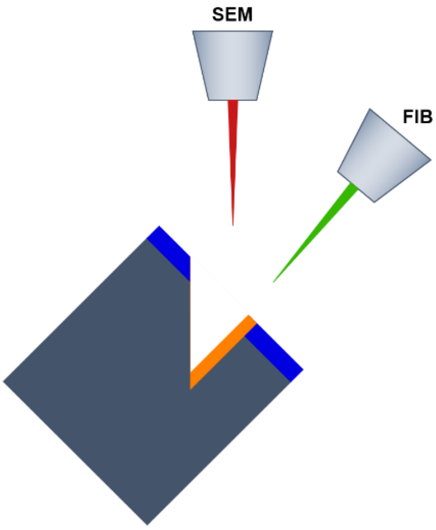

Figure 10 - A schematic representation of a focused ion beam scanning electron microscope. An image is made of the area (orange) using the SEM.

2.2.2. Composition

The composition of the depositions was characterized through energy dispersive X-ray (EDX) analysis and X-ray diffraction (XRD). EDX was performed in SEM (JEOL) using a 10 mm gun-to-sample distance, a 60-70 probe current (P.C.), 2,500x magnification, and > 4,000 counts per second (cps). Per sample, one measurement was performed. XRD measurements were taken of the full sample (deposit and substrate) and angles between 20° and 120° with a rate of 2°. The data was retrieved using PDXL-2 software and was plotted in Origin.

2.2.3. Electrochemistry

2.2.3.1. Capacitance (ECSA and wetting)

Capacitance was measured of pristine and treated Sigracet 39AA, Toray Paper, Freudenberg H23, ELAT Hydrophilic and AvCarb Felt. In the case of treated electrodes, they were first placed onto aluminum foil and oxidized under air in a box oven (Nabertherm) at 450 °C for 2. The carbon electrodes were clipped and immersed into the solution, assuring that the clip is not wetted.

Capacitance was measured in a three electrode cell containing a Pt wire CE, Ag/AgCl ref, and a 0.050 M H_2SO_4 electrolyte solution by immersing the porous electrodes and the geometrical surface area was measured. Cyclic voltammetry (CV) was performed between 0.2 and 0.45 V at eight different scan rates (10, 20, 50, 100, 150, 200, 300, and 500 mV s^{-1}) and the current was recorded.

By experimentally determining the electrochemical double layer capacitance (EDLC) the electrochemically active surface area (ECSA) of a porous electrode was estimated. Capacitance was measured using cyclic voltammetry (CV) where the electrode potential is swept between two limits and the current is recorded. If there are no Faradaic events observed (i.e. the current is independent of the applied potential) the voltammogram exhibits capacitive behavior (see Figure 11).

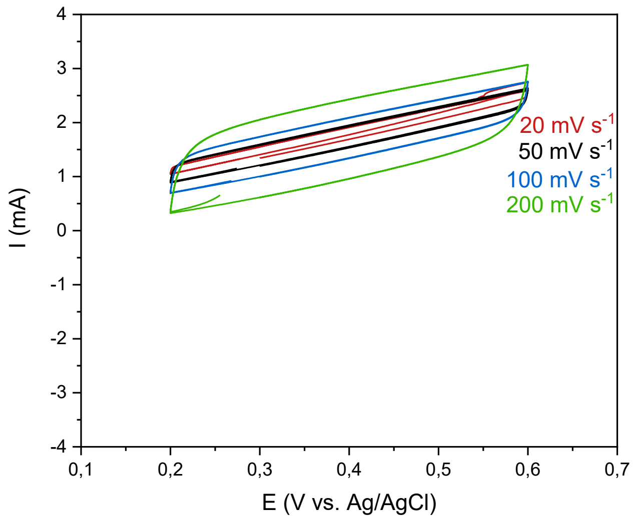

Figure 11 – Capacitive curves for multiple scan rates are presented. For increasing scan rate the difference of currents in the forward and backward direction increases.

The average capacitive current, i_{EDLC}, was calculated through the summation of the different currents at a fixed potential in the forward and backward direction of the cycle (i_+ and i_-) as [31], [32]:

$$i_{EDLC} = \frac{i_+ + |i_-|}{2} \tag{4}$$

The intensity of the current recorded increases linearly for increasing scan rate and by performing CV measurements for different voltage scan rates. The EDLC was calculated from the linear fit:

$$i_{EDLC} = EDLC\frac{dV}{dt} \tag{5}$$

The electrochemically active surface area was calculated as:

$$ECSA = \frac{EDLC}{C_{spec}m_e} \tag{6}$$

Where C_{spec} is the specific capacitance (F cm^{-2}) and m_e is the mass of the electrode (g). C_{spec} is an approximated constant of ≈ 18.0 ± 0.3 μF cm^{-2}. To obtain C_{spec}, CV measurements are performed on a polished glassy carbon electrode with a known surface area. A roughness factor of unity was assumed and is described by the ratio between the real surface area *vs* the geometrical surface area:

$$\rho = \frac{A_{real}}{A_{geo}} \tag{7}$$

Where A_{real} is the real surface area (cm^2) and A_{geo} is the geometrical surface area (cm^2). Substituting A_{real} with $m_e \times$ ESCA in equation (7), the specific capacitance can be calculated:

$$\rho = \frac{EDLC}{C_{spec}A_{geo}} \tag{8}$$

It is important to recognize that C_{spec} is an approximation, since carbon fibers and glassy carbon are expected to have differences in C_{spec}. The roughness factor was only measured in the case of carbon materials.

The capacitance measurements were used to indicate the wettability of the carbon electrodes. For an increase in ECSA and roughness factor, it is assumed that the wettability is improved for the electrode material.

2.2.3.2. Rotating disk electrode (RDE)

By conducting rotating disc electrode measurements, the diffusion coefficient was calculated for Cu^{2+} in 0.5 M H_2SO_4. A glassy carbon (GC) rotating disk electrode of 5mm in diameter was used. By rotating the electrode, the velocity of the electrolyte towards the surface depends only on the distance and not on the radial position or angle. Also, the smoothened surface of the electrode creates a uniformly accessible surface area so the mass transfer rate becomes constant as long as the bulk concentration does not change in time.

The diffusion coefficient shows a relationship between the rate of rotation and limiting current according to the Levich equation [33]:

$$i_{lim} = (0.201)nFAD^{\frac{2}{3}}\omega^{\frac{1}{2}}v^{\frac{1}{6}}C \tag{9}$$

Where I_L is the limiting Levich current (A), n is the number of moles of electrons transfer in the half reaction (-), F is the Faraday constant (C mol^{-1}), A is the area of the electrode (cm^2), D is the diffusion coefficient ($cm^2\ s^{-1}$), ω is the angular rotation rate of the electrode (rpm), υ is the kinematic viscosity ($cm^2\ s^{-1}$), and C is the analyte concentration (mol cm^{-3}).

The limiting current density (j_{lim}) is calculated from:

$$j_{lim} = \frac{i_{lim}}{A} \tag{10}$$

Then the j_{lim} versus square root of the angular rotation rate ($\omega^{1/2}$) can be plotted and results in a slope α, which is used to calculate the diffusion coefficient D as presented:

$$D = \left(\frac{\alpha v^{\frac{1}{6}}}{0.201nFC}\right)^{\frac{3}{2}} \tag{11}$$

2.2.4. Current efficiency

The current efficiency was determined by weighing the dry samples after the thermal pretreatment and cleaning treatment and before deposition to obtain the initial mass m_i (g) and after deposition and the post cleaning treatment to obtain the final mass m_f (g). The error margin of the weighing scale is ±0.0002 g.

The current efficiency CE% is the fraction of electrons that are dedicated to the deposited metal and this was calculated from the ratio of the measured mass over the theoretical mass:

$$CE\% = \frac{m_{meas}}{m_{th}} \times 100\% \tag{12}$$

The mass can be calculated from Faraday's law of electrolysis:

$$m_{th} = \frac{QM}{Fz} \tag{13}$$

Where Q is the total charge passed through [C], M is the molar mass of the deposited material [g mol^{-1}] (which is in this case M_{Cu} = 63.55 g mol^{-1}), F is the Faraday constant [C mol^{-1}], and z is the valency number of ions of the deposited material [-].

Chapter 3 - Electrodeposition of metals

3.1 Electrocrystallization

Electrodeposition is an electrochemical process where a chemical change is induced by the flow of an electrical current. An electrochemical cell is presented in Figure 12. The system requires two electrodes, an anode and a cathode, that are placed into a ionically conductive solution, the electrolyte. The potential difference between the electrodes is varied through an external power supply and induces electrons to move through the system. The anions in the electrolyte carry the induced current, completing the electrical circuit [32], [34].

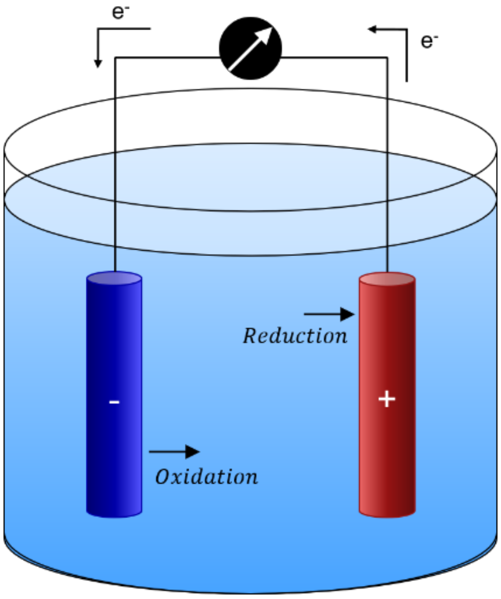

Figure 12 - An electrolytic cell consisting of an electrolyte solution in which two electrodes (anode and cathode) are immersed into. By applying the reduction potential, reduction and oxidation reactions happen on the cathode and anode, respectively.

Deposition of the metallic ions is induced by applying the associated reduction potential according to the Nernst equation (14). Through a heterogeneous electron-transfer reaction, the metallic ions migrate from the electrolyte towards the surface of the cathode and are deposited onto the cathode surface via a reduction reaction (15). An oxidation reaction occurs at the anode to maintain electrochemical neutrality. If the anode is soluble, the solution is replenished with metallic ions (16), however when the anode is insoluble, the electrolyte solution is oxidized (17) [35].

$$E_{red} = E^{\Theta}_{red} - \frac{RT}{zF} \ln Q_r = E^{\Theta}_{red} - \frac{RT}{zF} \ln \left(\frac{a_{Red}}{a_{Ox}} \right) \tag{14}$$

$$M^{n+} + ne^- \rightarrow M\ (s) \tag{15}$$

$$M(s) \rightarrow M^{n+} + ne^- \tag{16}$$

$$\frac{n}{2} H_2O\ (l) \rightarrow ne^- + nH^+ + \frac{n}{4} O_2\ (g) \tag{17}$$

In Figure 13 the electrocrystallization process is presented: in the bulk of the electrolyte, the metal ions are presented as hydrated metal ions. They are transported from the bulk towards the diffusion layer where the H_2O dipoles realign. The metal ion travels towards the double layer and reaches the outer Helmholtz plane (OHP) where the hydration layer is disposed. The metal ion adsorbs onto the surface reaching the inner Helmholtz plane (IHP) and is now an adatom that lies at the interface between the substrate and solution. When reaching the double layer, the adatom is subsequently incorporated into the crystal lattice. The newly created interface causes an increase in surface area and thus an increase in surface energy. Due to this excess in surface energy, the metal adatoms diffuses randomly on the substrate's surface. A cooperative process of agglomeration and growth of adatoms into a new crystal follows, initiating the electrocrystallization process and reducing excess surface energy. At a certain point, the thermodynamic formation energy of a cluster is larger than its surface energy and is considered a stable nucleus. It will continue to grow until the applied potential is no longer present [34]–[38].

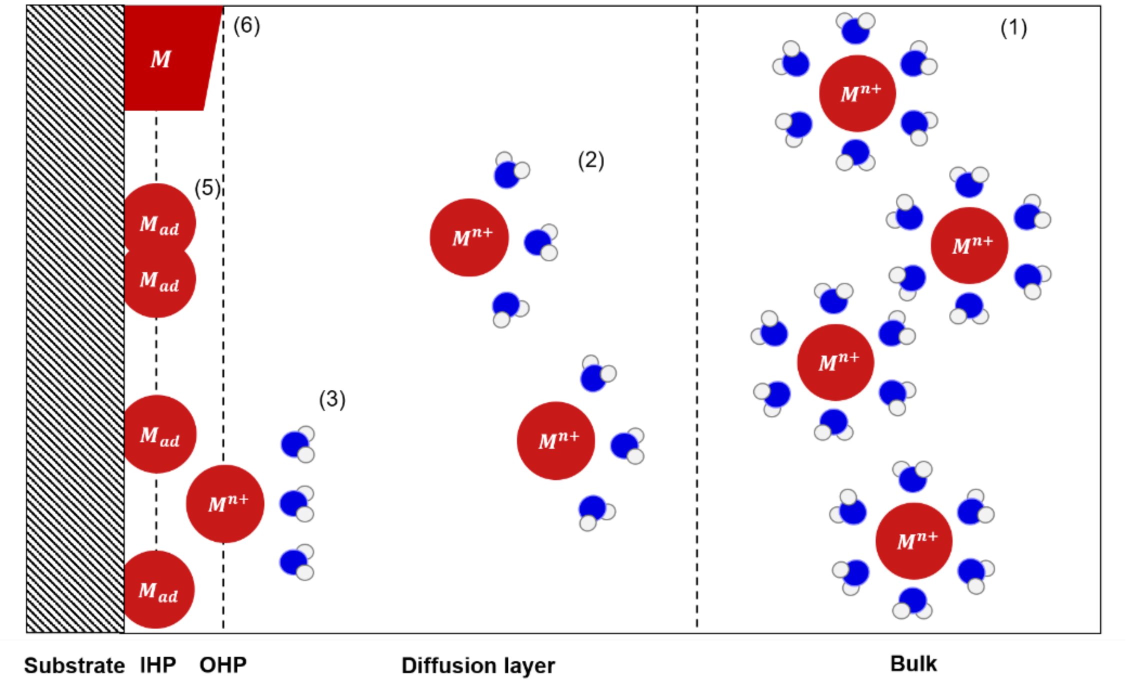

Figure 13 - Schematic of the electrochemical deposition process. (1) shows the hydrated metal ions in the bulk. When a potential is applied, the metal ions reach the diffusion layer (2) and the water molecules realign. The metal ion reaches the outer Helmholtz plane (3) and is subsequently adsorbed onto the surface when reaching the inner Helmholtz plane (4). The adatoms diffuse over the surface and agglomerate to clusters (5), initiating electrocrystallization (6). [35], [39].

In Figure 14, three different growth modes can be distinguished based on the interactions between the metal ions and the substrate. Case I is developed by Frank-van der Merwe, where the interaction between the substrate and the metal ions is stronger than in between the metal ions themselves [40], [41]. This leads to a two dimensional growth or layer-by-layer growth. This growth is usually observed for homogenous substrates. In case II, Volmer-Weber describe a growth mode where the adatoms are more tightly bound to each other than to the substrate. This induces island growth and results in a three dimensional morphology. This mode occurs more often when the substrate and the to-be deposited film are heterogenous in nature [42]. Case III describes a combination of the aforementioned cases: layer-by-island growth, Stranski-Kranstanov. Initially there is 2D growth and at a certain critical thickness the stress induced by the deposit results in 3D crystal growth.

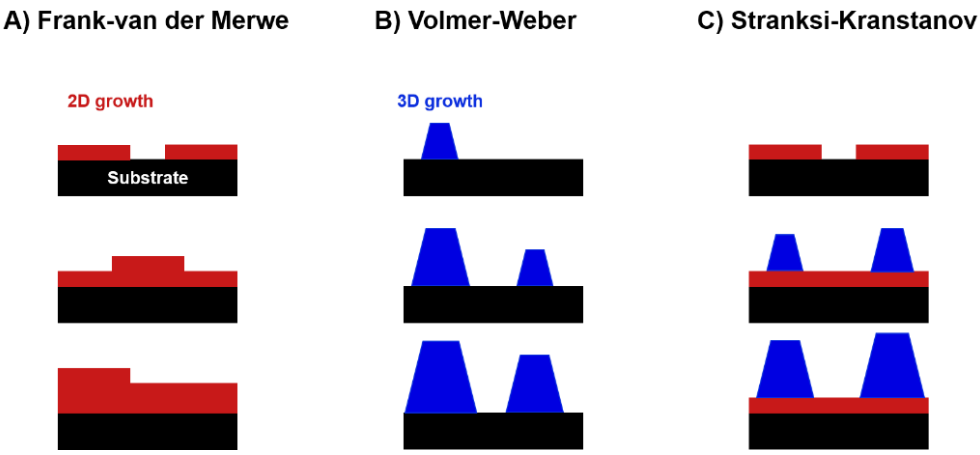

Figure 14 - The three growth modes: a) layer-by-layer growth that results in a two dimensional morphology, b) island growth that has a three dimensional morphology, and c) a combination of layer (2D) and island growth (3D) [43], [44].

3.2 Electrode charge-transfer and mass transport

The general formula for mass transport of species i along any directions is given by the following equation:

$$J_i = -D_i \nabla c_i - \frac{z_i F}{RT} D_i c_i \nabla + \bar{v} c_i \tag{18}$$

Where J_i represents the flux of species i [mol cm^{-2} s^{-1}]; D_i is the diffusion coefficient of species i [cm^2 s^{-1}]; z_i is the charged of species i [-]; c_i is the concentration of species i [mol cm^{-3}]; $\bar{v}$ is the vector sum of the fluid velocity in the three Cartesian coordinates; ∇ is the Laplace operator for the vector sum of the inner potential gradients. The three terms represent the diffusion the migration, and the convection of the system, respectively. Diffusion should always be considered, because the consumption of species at the electrode surface forms/induces a concentration gradient between the concentration near the surface of the electrode and the bulk of the solution. This is the driving force for reactant species to move towards the surface of the electrode, because the product species leave the from the solution into the interface (i.e. the species are removed from the solution, Figure 13 – step 6). Migration is the mass transport that is driven by the inner potential gradient of the solution near the electrode and should also be considered. The charge transfer during electrodeposition results in a change of the charge balance close to the electrode. A consequence of the process of charge transfer is the depletion and production of electroactive species close to the electrode. This evokes a mass gradient between the bulk solution and the solution near the electrode. Therefore mass transport and charge transfer through diffusion are synergistic since both processes support each other.

The electrodeposition method is used in this thesis to fabricate novel porous electrodes. In the following chapters, we elaborate on the theory of electrodeposition of copper, nickel and NiCu alloy coatings. Also, a literary study is done on current investigations regarding the electrodeposition of the metals and the results with corresponding discussions are presented.

Chapter 4 - Electrodeposition of copper

4.1 Introduction on copper electrodeposition

Copper electrodeposition is widely used in industrial processes such as copper refining, electroforming, and plating, and plays an important role in semiconductor interconnect technology where it has replaced aluminum. Cu is electrodeposited for a wide range of applications due to its mechanical and physical properties, i.e. it is used for interconnects in integrated circuits due to its high electrical conductivity. Cu also has a high plating efficiency, resulting in excellent coverage. In addition, Cu is used as an underplate layer to level rough substrates and is a relatively inert compound in most plating solutions when other metals are present [45]. Copper is a soft metal and can be used as a thermal expansion barrier by absorbing stress produced when metals with different thermal expansion coefficients undergo temperature changes and it is inexpensive to buff copper since it is so soft.

Acid copper is the most used solution for copper plating, replacing most of the pyrophosphate solutions while still being able to deposit copper at very high current densities, but being less expensive, easier to control, and less susceptible to impurities [45].

The first stages of the formation of a copper deposit depend on the deposition rate, substrate surface nature, and deposition technique. The final stage in the growth involves an equilibrium of copper electrochemically dissolving and precipitating. The character of the copper deposit is influenced by the concentration of the Cu salts, additives, free acid, temperature, cathode current density, and the nature and degree of agitation.

Copper deposition from acid solutions involves the following deposition reaction sequence when chloride is present in solution to stabilize Cu^+:

$$Cu^{2+} + e^- \rightarrow Cu^+ \quad E^0_{Cu^{2+}/Cu^+} = 0.16\ V\ vs. SHE \tag{19}$$

$$Cu^+ + e^- \rightarrow Cu\ (s) \quad E^0_{Cu^+/Cu} = 0.52\ V\ vs. SHE \tag{20}$$

If there are no chloride ions present, only one reaction occurs and Cu^{2+} is not stabilized:

$$Cu^{2+} + 2e^- \rightarrow Cu\ (s) \quad E^0_{Cu^{2+}/Cu} = 0.34\ V\ vs. SHE \tag{21}$$

The electrodeposition of copper is of interest for VRFB to enhance the electrocatalytic activity of the electrode. In the next section, a more in depth literature study is provided on the electrodeposition of copper onto 3D scaffolds.

4.1.1. Electrodeposition of copper onto 3D scaffolds

A challenge within the research into the deposition of copper in three dimensional structures is to obtain a proper distribution of Cu (nano)particles throughout the full electrode structure due to limited migration and diffusion towards the bulk of the electrode. In literature, many approaches have been taken to develop novel electrodeposition techniques to plate 3D substrates.

A factor of importance to assure homogeneous deposition is wettability. As mentioned in a study on electrode microstructure, current techniques to improve the wettability for aqueous RFBs is done through surface modification of the carbon electrodes [31]. For example, in another study thermal pretreatment has shown an improvement in wetting, due to the increase in oxygen content at the electrode surface that facilitates charge transfer and increases the hydrophilicity of the electrode [27].

In the work of Wainright et al, focus lies on the fabrication of a homogeneous copper deposition using a flow battery to prevent depletion of the copper concentration in the bulk of the electrode [46]. Copper is electrodeposited into porous carbon felt electrodes (thickness of 4 mm) during charging of the flow battery. A copper-iron sulfate chemistry was used because the potential of the plating solution at the negative electrode is 0.46 V vs. SHE and therefore HER can be prevented. Deposition occurred during charging where Cu was deposited in the porous negative electrode. This study showed that the choice of electrolyte influences the plating utilization (i.e. the volume of the electrode that is plated with copper). In more acidic solutions containing H_2SO_4 instead of Na_2SO_4, the conductivity of the electrolyte increases and the plating utilization increases from 12% to 23%. In addition, a 50% increase in deposit was found when the applied current density was decreased from 140 to 60 mA cm^{-2}. They argued that the current distribution changes for different applied current densities.

In 2016, Wei et. al also used a flow battery setup for the electrodeposition of Cu nanoparticles (NPs) onto graphite felt electrodes [28]. The Cu nanoparticles significantly increase the electrochemical kinetics of the V^{3+}/V^{2+} redox reaction. 5 mM Copper(II) sulfate was added to the electrolyte and reduced at the electrode. The deposited copper only functions as a catalyst for the V^{3+}/V^{2+} due to the reduction potential of Cu^{2+}/Cu^0 (0.143 V vs. Ag/AgCl) being reached before V^{3+}/V^{2+} (-0.457 V vs. Ag/AgCl). The energy efficiency increases from 62.3% for the pristine electrode to 80.1% for the decorated electrode. Additionally, the discharge capacity increased from 30.6% to 83.7% of the theoretical capacity. The stability of the decorated electrode appeared to decrease only 0.23% per cycle over 50 cycles and therefore suggests that the addition of Cu NPs is a promising technique to improve the performance of VRFBs.

Another approach to improve the diffusion and migration of metallic ions into the pores is through pulsed electrodeposition as mentioned in previous studies [47]–[50]. A study was conducted by Nielsch et al. fabricated uniform Ni deposit into ordered Al pore structures through pulsed electrodeposition (PED). This paper is of interest due to the similarities between the properties of Ni and Cu and therefore we suspect we can learn from each other. In here, PED was found to be a reliable method for electrodeposition into porous structures since it is able to compensate for the slow diffusion-driven transport of metal ions through the pores. Alternating current (ac) pulses were applied to allow better control over the deposition rate and ion concentration at the surface of the porous structure. It is mentioned here that when the rate of ED is higher than the transport rate through the pores, the metal ion concentration decreases at the bottom of the pores. It causes HER to become dominant, inhibiting homogeneous deposition and decreases the pore filling factor and the current efficiency. So, deposition is based on modulated pulse signals. Relatively high current densities are applied during PED, which increases the number of deposition centers in each pore. The deposition pulse is followed by a short positively polarized pulse to discharge the capacitance of the barrier layer and to interrupt the electric field at the deposition interface/to repair the discontinuities in the barrier layer. An off time is used to recover the concentration of ions at the deposition interface and therefore improving the homogeneity of the deposit and limiting HER. Nearly 100% of the pores ($h = 1$ μm) could be filled with Ni deposit and about 90% of the pores are filled. At shorter off times, wire growth is more pronounced and the size is decreased. Also, the formation of hydrogen bubbles is observed for these shorter off times. This may be due to the depletion of metal ions concentration at the deposition interface, which increases HER and disturbs the diffusion of ions into the pores. Therefore not all pores are filled with Ni and the nanowires are of different lengths. A sufficiently long deposition time ensures uniform filling of the pores, since there is less to no depletion of metal ions at the deposition interface and ions are able to transport through the pores. When the off time is too large, the deposit can be peeled off due to a side reaction between the oxide and the electrolyte [44].

We hypothesize that the electrocatalytic activity for VRFBs can be increased by introducing copper particles that function as a catalyst. A homogeneous copper coating on 3D scaffolds is expected to be obtained through pulsed electrodeposition, to reduce the depletion of ions near the surface and to aid the diffusion of ions towards the bulk of the scaffold.

4.2 Results and discussion

In Figure 15, a cyclic voltammogram of 1 mM $CuSO_4$ with and without the addition of 0.5 M KCl to stabilize Cu^+ is presented. For $CuSO_4$ without KCl one anodic peak and one cathodic peak are measured at 0.446 V and -0.223 V, respectively. A thin orange deposit was found plated on the working electrode after performing the CV. This observations might indicate that a two electrons transfer process occurs, which is Cu^{2+}/Cu^0 as seen in literature [51]. The shape of the peak suggests that the transition appears to be sluggish, and this indicates that there is some resistance present which probably comes from the low analyte concentration with no supporting salt [52]. An electrochemical impedance spectroscopy measurement could have been performed to extract the ohmic drop generated by the solution resistance.

For $CuSO_4$ with KCl present in solution, two anodic and two cathodic peaks are visible. This indicates that two single-electron transfer processes occur subsequently: Cu^{2+}/Cu^+ and Cu^+/Cu^0. The anodic peak around -0.011 V is the oxidative stripping of Cu^0 to Cu^+ and the anodic peak around 0.228 V is the oxidation of Cu^+ to Cu^{2+}. The cathodic peaks at 0.149 V and -0.272 V are the reduction of Cu^{2+} to Cu^+ and Cu^+ to Cu^0, respectively. For the transition of Cu^{2+}/Cu^+, the shape of the CV has similar peak sizes and corresponds to a reversible reaction (with a peak separation of 261 mV). In the case of Cu^+/Cu^0 a nucleation loop is present. A nucleation loop occurs when the current is higher for the backward scan [53].

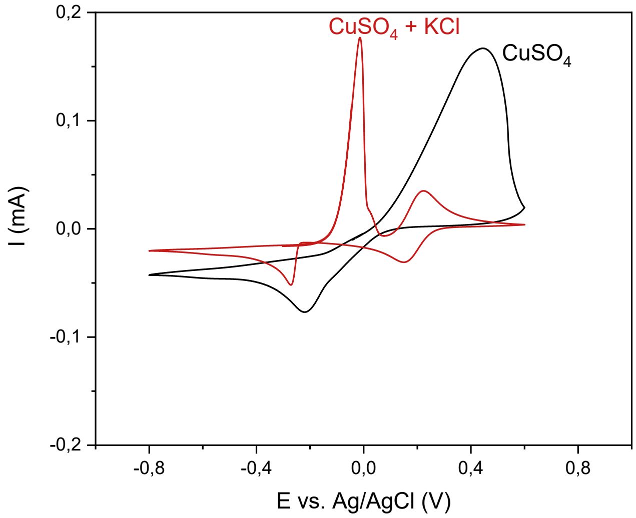

Figure 15 - A cyclic voltammogram is shown for CuSO$_4$ with and without the addition of KCl to stabilize Cu$^+$.

In Figure 16a, a linear sweep voltammogram is presented for different rotational speeds of the working electrode (GC). A solution of 1 mM CuSO$_4$ in 0.5 M KCl was used for the measurements and the rotation speeds of the GC electrode were 200, 400, 800, 1000, and 1400 rpm. The values for i_{lim} were taken at 0 V. The current density j_{lim} was calculated from eq. (10) and plotted vs. $\omega^{1/2}$ as is seen in Figure 16b. The diffusion coefficient is calculated from eq. (11) and yields a value of 52.32 × 10^{-6} cm^2 s^{-1}. In literature a value of 6.8 × 10^{-6} cm^2 s^{-1} was found for 1.96 mM CuSO$_4$ in 0.5 M KCl at 24.95 C° [54]. A comparison of these values suggests that our experimental value is an underestimation of the diffusion coefficient mentioned in literature. This could be explained by the fact that for high rotation speeds, the limiting diffusion plateau is not yet reached and therefore the experimental slope is smaller than the expected slope.

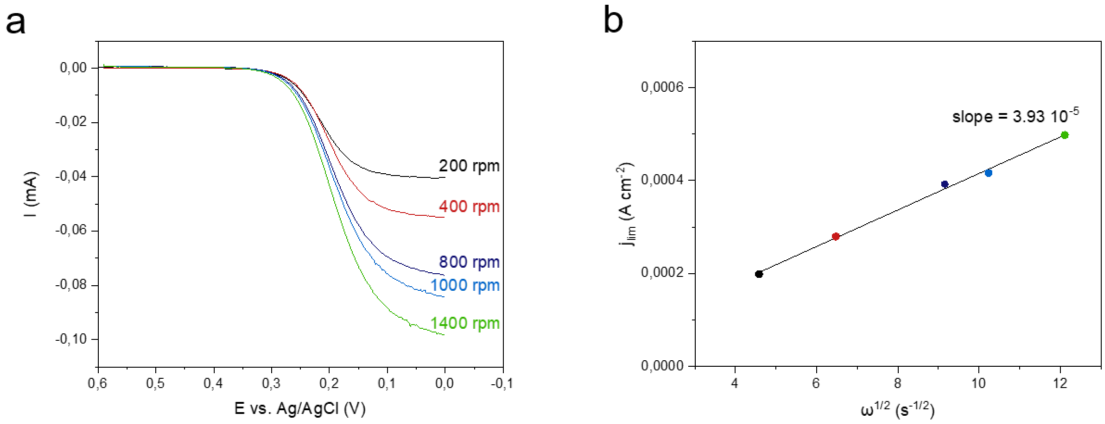

Figure 16 – a) A linear sweep voltammogram is given at different rotational speeds of the GC electrode. b) the limiting current density (j_{lim}) vs. the square root of the angular speed ($\omega^{1/2}$) is plotted and the slope is subtracted from the plot.

In the following sections, deposition of copper onto Ni foil was studied. This is of interest for the electrodeposition of NiCu films onto Ni foil. Then, the electrodeposition of copper onto graphite foil is used to get an insight in the mechanism of deposition for a 2D system. This knowledge is used and translated to 3D carbon electrodes in the last section on Cu electrodeposition on ELAT hydrophilic and Freudenberg H23.

4.2.1. Deposition of Cu onto flat Ni surface

Copper films were fabricated using different solutions with varying pH values. Two solutions of 0.1 M $CuSO_4$ in either 0.5 M Na_2SO_4 or 0.5 M H_2SO_4 was used to create copper films on Ni foil using a fixed current of -18 mA. The deposition time was varied to obtain three solutions with different pH: 10 minutes and 1 hour for the sodium sulfate solution and 1 hour for the sulfuric acid solution, resulting in pH values of 5, 3, and 1, respectively. The pH was measured after deposition. In Figure 17a, the copper deposits that were obtained through electrodeposition are shown for the three pH values and a change in the color of the deposit is observed. This change of deposit color is investigated to determine the nature of the deposit. In Figure 17b a Pourbaix diagram is presented for copper at 25 °C [55]. A Pourbaix diagram is a potential vs. pH diagram that presents the stable phases of an aqueous electrochemical system at a certain concentration and is based on Nernst equations to create the areas of corrosion and passivation. From the Pourbaix diagram, the nature of the deposit can be estimated. In our case, the equilibrium potentials during electrodeposition are -0.097, -0.047 and -0.103 V vs SHE for pH of 5, 3, and 1, respectively. This relates to potentials that might result in the formation of copper oxides and passivation of the deposit. Another explanation might be the formation of a porous deposit. Both explanations are supported by the brittle and powdery nature of the deposit, which is easily removed. Other techniques like powder X-ray diffraction (XRD) and X-ray photoelectron spectroscopy (XPS) could be used to validate the nature of the deposits, however, they were not at our disposal during this period and therefore we decided to continue with the solution that resulted in the bright copper deposit which had a pH of 1. However, to determine the nature of the deposit, powder XRD could be performed if the distinct peaks for copper and copper(I) oxide and copper(II) oxide are known. Also, XPS should tell whether a chemical shift is visible that indicates the existence of a different oxidation state of copper and therefore the formation of oxides in the deposit.

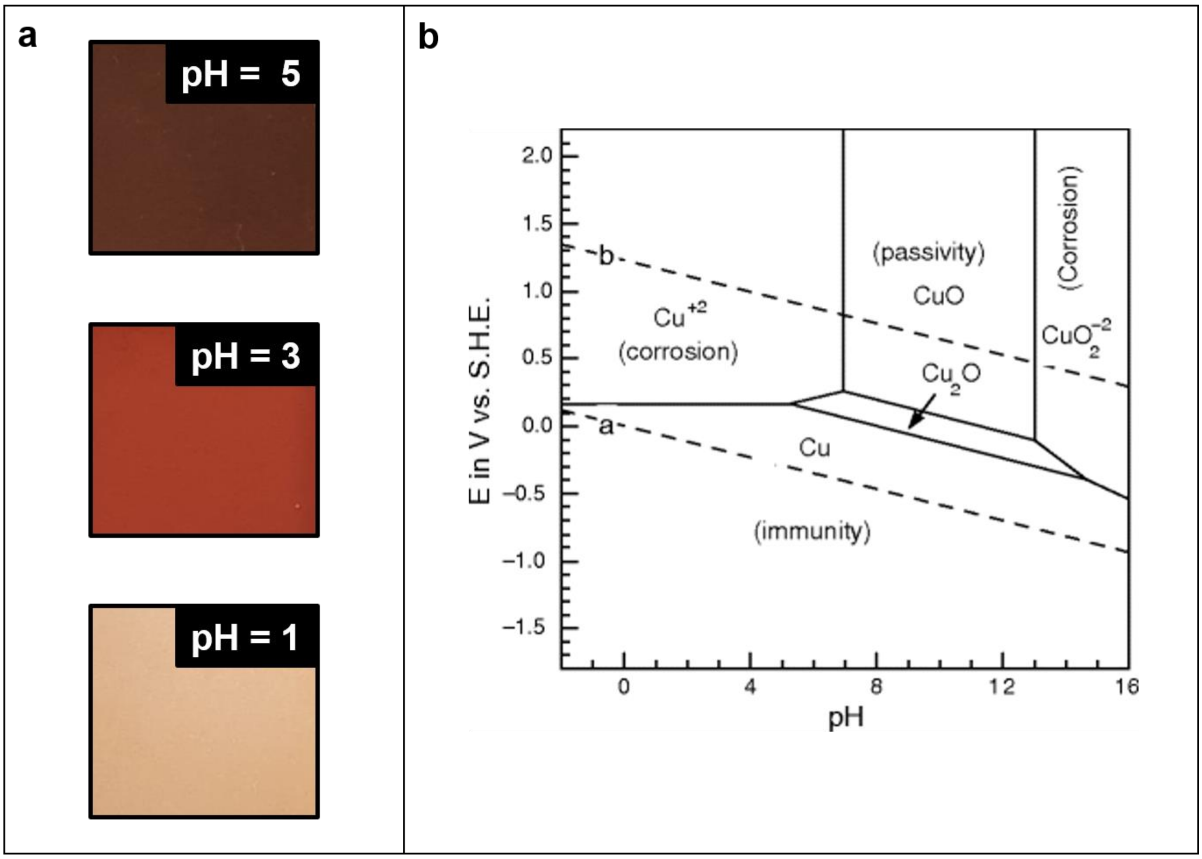

Figure 17 - a) the copper deposits are presented for different pH levels of the solution. b) a Pourbaix diagram is shown for Cu at 25 °C. Adapted from E. McCafferty, 2010.

A better control of the deposition can be achieved by current controlled electrodeposition compared to the previous potential controlled electrodeposition. From current controlled experiments, the current efficiency can be determined by either comparing the masses of the working electrode (substrate) before and after deposition or comparing the thickness of the deposit layer before and after deposition. In Figure 18a, a SEM image of a bright copper deposit on Ni foil is shown. The deposit was obtained from a solution containing 0.1 M $CuSO_4$ in 0.5 M H_2SO_4 and the applied current was -18 mA for 1 hour. A different morphology is observed for the copper layer compared to the Ni foil and grain boundaries are visible in the deposit.

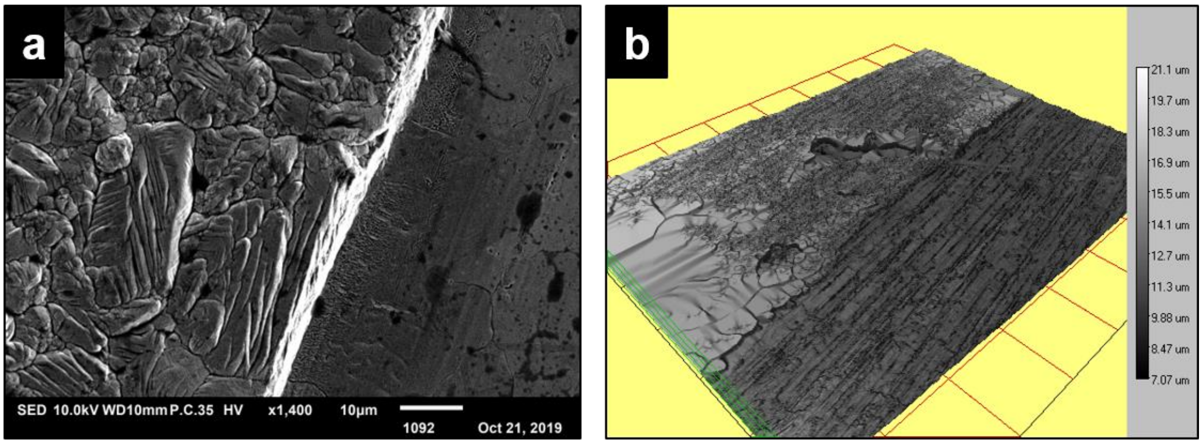

Figure 18 – a) SEM image of Cu deposit (left) on Ni foil (right) and b) a visualization of the sample using an interferometer with a scale ranging from 7.07 to 2.1 μm.

The thickness of the deposit was determined using a interferometer (BRAND) and the result is shown in Figure 18b. According to Figure 18b, the Cu film has an average thickness of 8.325 μm. To determine the current efficiency in the case where the thickness of the deposit is known, the ratio of the measured and theoretical thickness is taken. The approximated thickness h can be calculated theoretically:

$$h = \frac{m}{\rho A} \tag{22}$$

Where m is the theoretical mass [g] of the deposit, ρ is the density [g cm^{-3}] of the deposited material, and A is the area [cm^{-2}] where the film is deposited. The theoretical mass is calculated using Faraday's law of electrolysis (eq. (13)). The theoretical thickness that could be achieved is 8.758 μm. Comparing the practical and theoretical thicknesses implies that the current efficiency (CE%) is 95.1%.

A FIB-SEM was used to make a cross section of the Cu film on Ni foil to see what the bulk of the deposit looks like. The cross section is presented in Figure 19a. The thickness of the deposit can be determined using a ruler on top of the SEM image, since a border is visible between the Ni substrate and the Cu film. The thickness was found to be ~3.7 μm. The thickness of the layers is also measured using the EDS software of the SEM and is presented in Figure 19b. Here, the thickness is estimated from the atomic percentages measured of each metal and is estimated to be ~ 4 µm. It must be noted that the sample used for FIB-SEM had a deposition time of 30 minutes and therefore the theoretical height that could be achieved is 4.121 µm. The CE% in this case lies between 89.8% and 97.1%.

Being able to obtain proper cross sections is evident if one wants to investigate the bulk of a metallic (porous) electrode. FIB-SEM has proven to be an adequate way to obtain a clean cross section for solid metals.

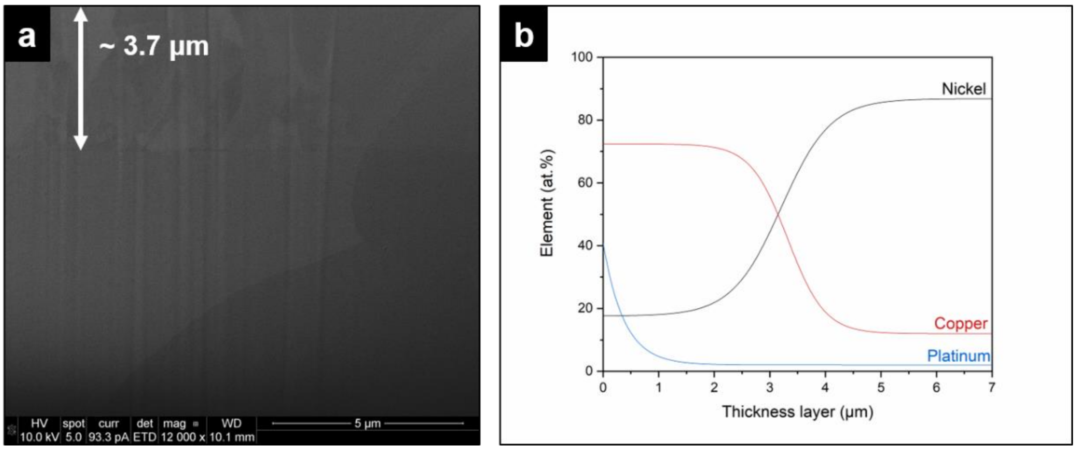

Figure 19 – A FIB is used to create a cross section and a SEM image is presented that shows the bulk of the deposited layer in the top.

4.2.2. Deposition of Cu onto graphite foil

4.2.2.1. Potentiostatic electrodeposition

The electrodeposition of copper onto graphite foil was investigated. The goal was to obtain a conformal deposit through electrodeposition from a solution containing 0.1 M $CuSO_4$ in 0.5 M H_2SO_4 at different current densities. Different deposition times were taken (t_{dep} = 25 s, 50 s, and 250 s) for four different currents with a fixed area of 1 cm^2 to obtain a set of current densities (i = -50 mA cm^{-2}, -100 mA cm^{-2}, -150 mA cm^{-2}, and -200 mA cm^{-2}). The goal of these experiments was to gain some insight in the nature of the different deposits and the efficiency of the ED process.

In Figure 20, the results are presented for the Cu electrodeposition with t_{dep} = 250 s. In Figure 20a, the potential vs. time curves are shown for the different currents applied. A drop towards more negative potentials is observed. The drop in potential occurs faster for more negative current densities. An explanation for this behavior might be the depletion of Cu^{2+} near the surface of the substrate. At -0.6 V and lower, HER begins to evolve which could compete with the deposition of copper. This can be supported by the CE% presented in Figure 20b, where values are observed <100%. During electrodeposition, a current is measured over time and indicates that a reaction occurred. A value below 100% indicates that side reactions took place during deposition. If Cu^{2+} is not reduced, it must be the solvent that gets reduced instead. When water is consumed a lower mass is deposited and therefore a lower CE% is found.

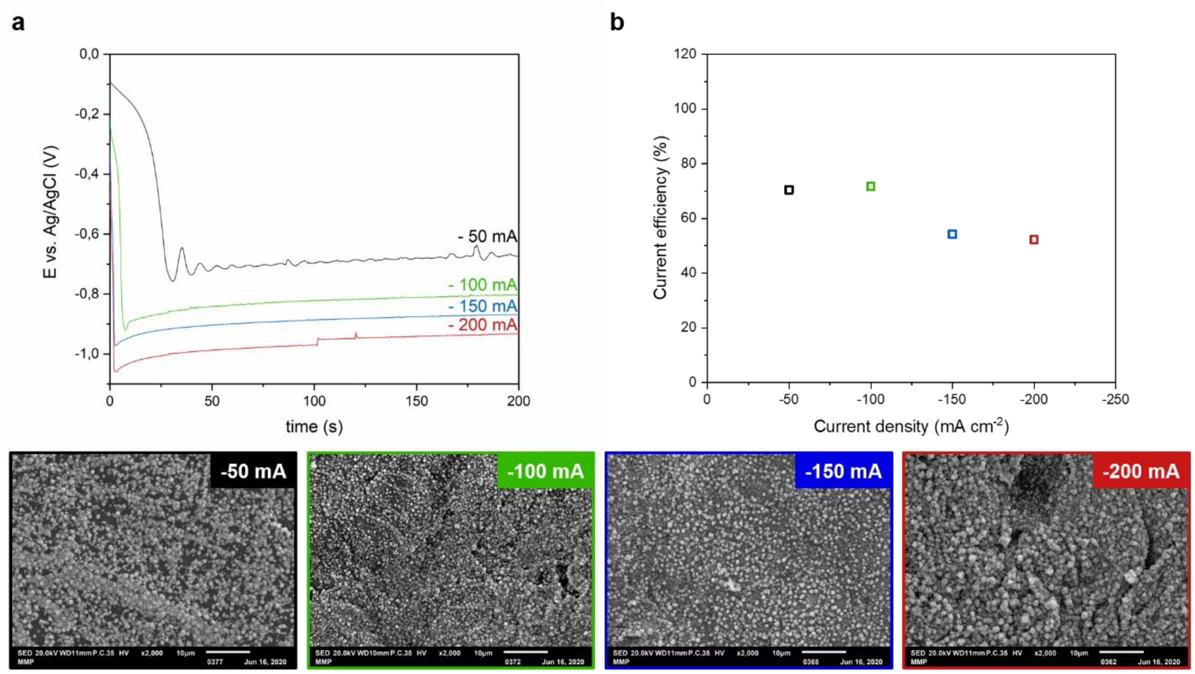

Figure 20 - The results are presented for electrodeposition of Cu from 0.1 M $CuSO_4$ in 0.5 M H_2SO_4 and a t_{dep} of 250 s. In a) the potential vs. time curves are given for the different currents that were applied. In b) the current efficiencies vs the current densities applied are presented. In the bottom, the SEM images are presented of the deposits for the different currents.

The SEM images in Figure 20 were taken of an area in the bulk of the deposit and show full coverage. Also, the deposit appears to be very uneven which could be caused by the formation of hydrogen bubbles at negative deposition potentials and therefore lead to the formation of pores in the deposit. In addition, the large nucleation overpotential results in island growth that is under mixed kinetic/diffusion control. This results in the formation of hemispherical islands [56], which are observed in the SEM images.

A drop in the potential is unfavorable since it evokes HER and therefore two solutions were explored: 1) using pulsed electrodeposition, and 2) increasing the concentration of copper in the electrolyte. It is hypothesized that both solutions decrease the depletion of copper ions near the surface of the substrate which fosters Cu^{2+} activity over H_3O^+.

4.2.2.2. Pulsed electrodeposition

First, pulsed electrodeposition of copper from the same solution (0.1 M $CuSO_4$ in 0.5 M H_2SO_4) was performed. For pulsed deposition, three parameters are introduced during deposition, which are the cathodic pulse, anodic pulse and off time (see Figure 21). The anodic pulse time t_a and off time t_{off} were fixed at 2 ms and 1 s, respectively. The cathodic pulse time t_c was varied (0.05 s, 0.1 s, and 0.5 s). The same four current densities were used as in the previous experiment with direct current (dc) deposition (-50 mA cm^{-2}, -100 mA cm^{-2}, -150 mA cm^{-2}, and -200 mA cm^{-2}). The magnitude for the cathodic and anodic pulse were e.g. ± 50 mA cm^{-2} and no current was applied during the off time (i = 0 mA). A total of 500 cycles were performed so total charge would be comparable to the total charge of dc electrodeposition (t_{dep} = 250 s). Since the t_a is so small (2 ms), the decrease in total charge during deposition is negligible.

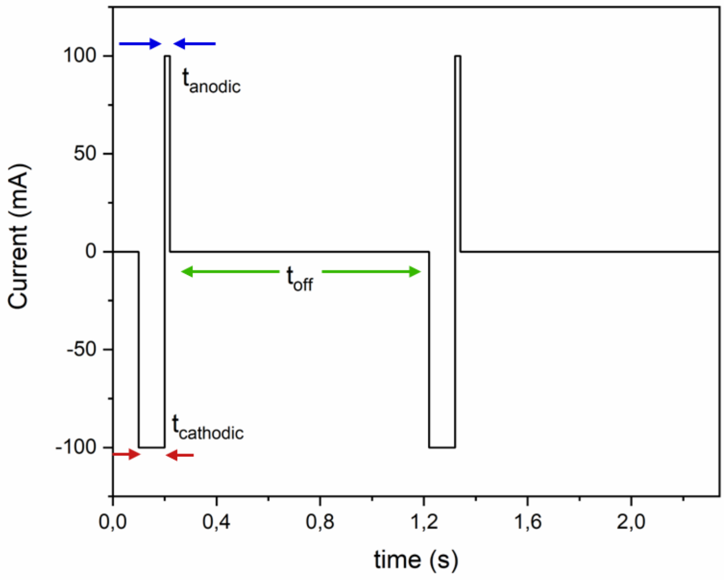

Figure 21 - The layout for PED with a cathodic pulse (t_c), an anodic pulse (t_a), and an off time (t_{off}).

In Figure 22, the results are presented for t_c = 0.5 s. In Figure 22a, there is still a large potential drop visible for currents < -100 mA, however the average value has increased by +0.2 to +0.3 V compared to dc electrodeposition (Figure 20a). For -50 mA, the potential deviation is much less prominent compared to the others. In Figure 22b, the CE% vs. current density is presented and there are two distinctive features. The first being the CE% at -50 mA cm^{-2}, which has a value of 26.7%. An explanation for this behavior is that the deposition potential has not reached the reduction potential of Cu^{2+} effectively. The applied anodic pulse of +50 mA cm^{-2} is suggested to be large enough to dissolve the readily deposited Cu. Therefore less copper is deposited resulting in a lower CE%. The second feature to discuss is the CE% at -100 mA cm^{-2} that has a value >100%. A thorough explanation for this is given at the end of the results of this section, since this is seen in later experiments as well.

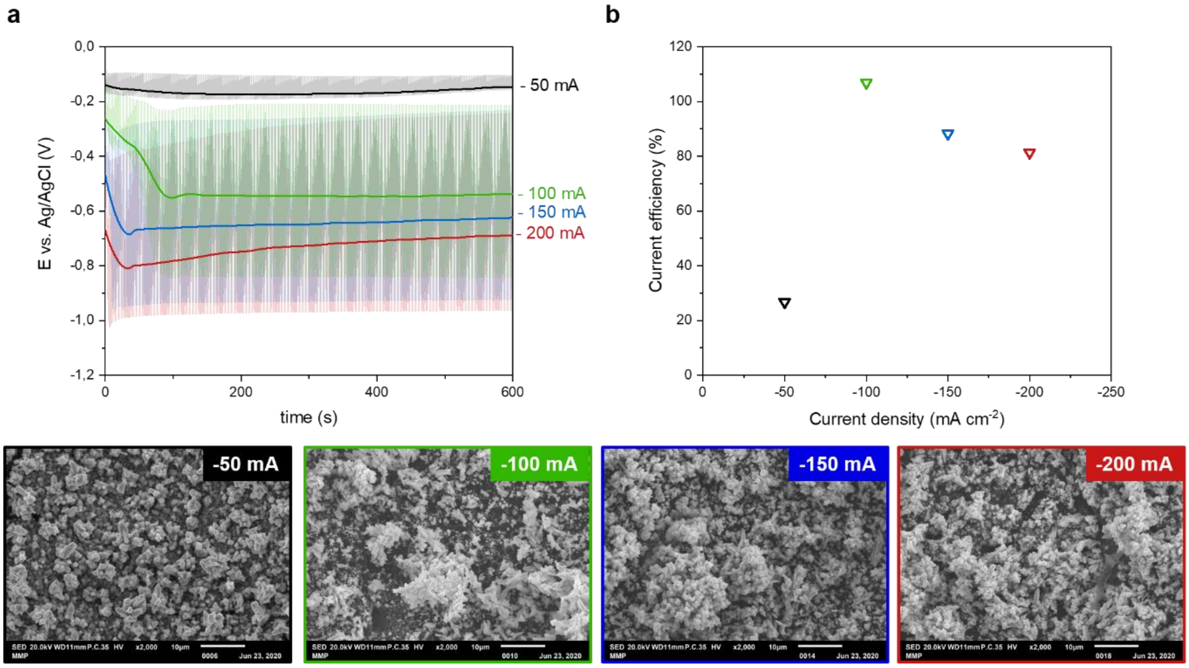

Figure 22 – The results are presented for pulsed electrodeposition of Cu from 0.1 M $CuSO_4$ in 0.5 M H_2SO_4 and a t_c of 0.5 s. In a) the potential vs. time curves are given for the different currents that were applied. In b) the current efficiencies vs the current densities applied are presented. In the bottom, the SEM images are presented of the deposits for the different currents.

Comparing the CE% of pulsed and dc electrodeposition (Figure 20b), the current efficiency appears to improve for pulsed electrodeposition. This indicates that more Cu^{2+} is reduced and suggests that the off time provides a replenishment of Cu^{2+} near the surface of the substrate.

The morphology of the deposit is presented in the SEM images of Figure 22 and were taken of the bulk of the deposit. All images show the formation of aggregates and dendrites. An explanation for these features is the formation of hydrogen bubbles during electrodeposition. The deposition potential decreases to values of -0.9 V and here HER occurs. In addition, a large nucleation overpotential favors the formation of dendrites since the island growth of the deposit becomes diffusion controlled [56].

The second approach to improve copper electrodeposition is investigated. A solution with a higher concentration of copper was used consisting of 1.25 M $CuSO_4$ in 0.5 M H_2SO_4. In Figure 23, the results are presented for t_{dep} = 250 s. In Figure 23a, the potential vs. time curves are shown and the potential drop that was observed in Figure 20a is significantly reduced. In Figure 23b, the CE% vs. current densities are presented and show 100% CE in each case.

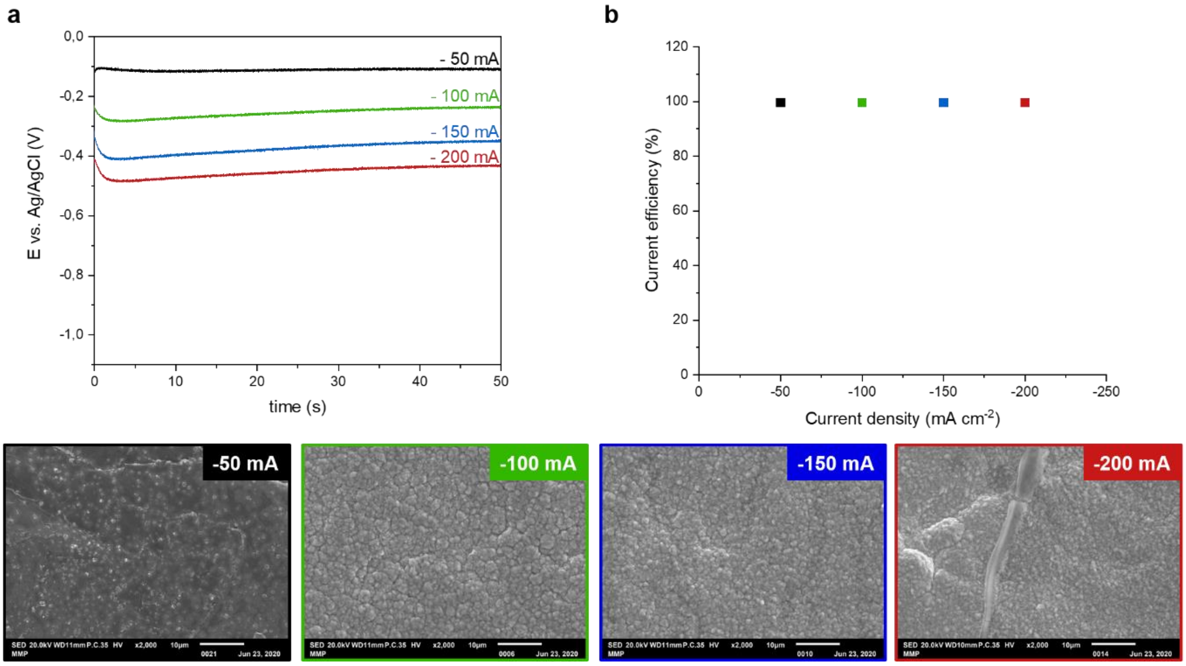

Figure 23 - The results are presented for electrodeposition of Cu from 1.25 M $CuSO_4$ in 0.5 M H_2SO_4 and a t_{dep} of 250 s. In a) the potential vs. time curves are given for the different currents that were applied. In b) the current efficiencies vs the current densities applied are presented. In the bottom, the SEM images are presented of the deposits for the different currents.

The SEM image in Figure 23 show a similar morphology for each applied current. In the cases of -100, -150, -200 mA, the nucleation overpotential is close to the equilibrium potential (E_{eq} = -0.310 V). This relates to island growth that is under mixed kinetic/diffusion control [56]. For more negative applied currents, the nucleation overpotential becomes larger and the grain sizes of the deposit become smaller. In addition, the lower applied currents are closer to kinetic control and go towards diffusion control for increasing applied current. This is linked to the grain size which becomes smaller if the island growth is diffusion controlled, resulting in hemispherical features. The grain size increases when the island growth is closer to kinetic control, resulting in larger island shapes.

Comparing the morphology of the deposits of 1.25 M to 0.1 M $CuSO_4$ (Figure 20), a higher concentration appears to improve the homogeneity of the deposit. This is addressed by the increase in island growth lead by kinetic control due to a smaller nucleation overpotential.

Finally, both solutions are combined in which pulsed electrodeposition is performed using a high concentration of copper (1.25 M) and the results are presented in Figure 24. In Figure 24 a, the potential drop is less prominent and similar to Figure 23a.

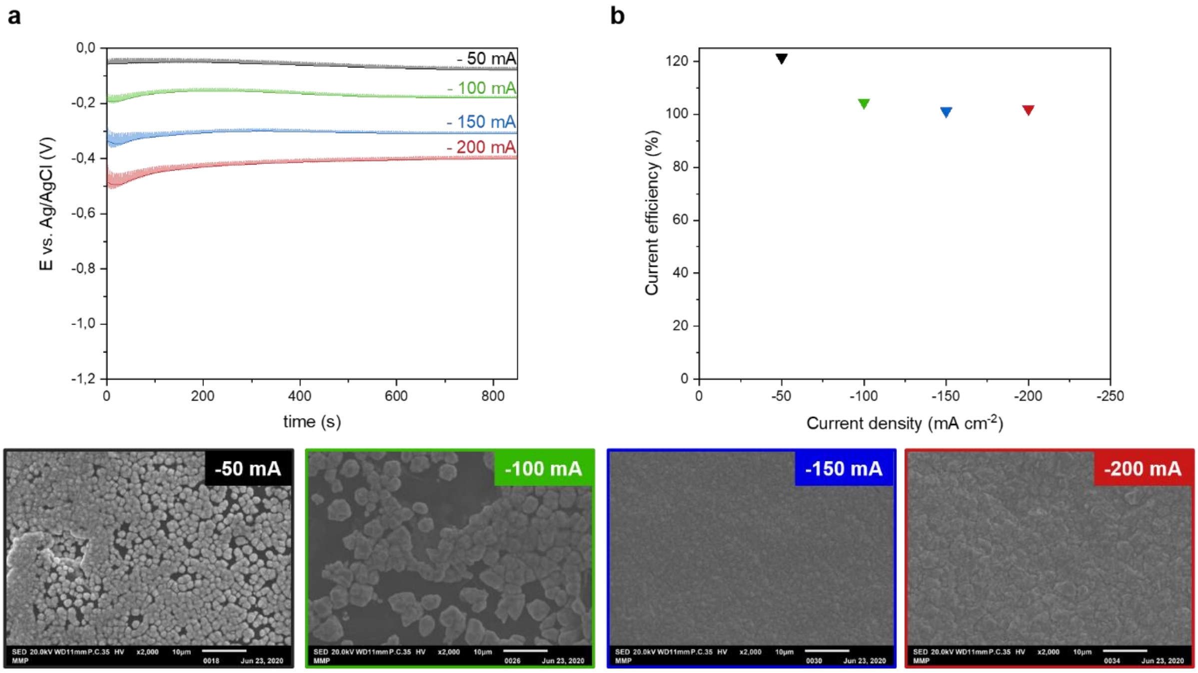

Figure 24 - The results are presented for pulsed electrodeposition of Cu from 1.25 M $CuSO_4$ in 0.5 M H_2SO_4 and a tc of 0.5 s. In a) the potential vs. time curves are given for the different currents that were applied. In b) the current efficiencies vs the current densities applied are presented. In the bottom, the SEM images are presented of the deposits for the different currents.

The SEM images in Figure 24 show that the morphology appeared to improve compared to the previous experiments for -150 mA and -200 mA. Hemispherical islands are seen in the images for -50 mA and -100 mA, indicating a growth of mixed diffusion and kinetic control. The deposit appears to be quite conformal in the case of -150 mA, whereas for -200 mA, grain boundaries become more eminent.

It should be noted that for some experiments CE% values of >100% were observed. The reason for this behavior can be attributed to several factors and these were investigated. The first explanation is an improper cleaning procedure after deposition. Samples may contain copper sulfate salts after deposition, therefore the cleaning is eminent to obtain proper CE% values. Experiments that appeared to be inconsistent in their CE% values were performed again and the cleaning procedure was adjusted to assure no salts were found. This was then confirmed by performing ESD measurements to see if any sulfur (indicating there is sulfate present in the deposit) was still there. Even after obtaining samples that appeared to have no sulfur in their deposits, CE% were found to have >100%. Another explanation that causes a CE% >100% is the entrapment of salts during deposition. Graphite foil exists of sheets and therefore has some slants and cuts on its surface where salts get entrapped. In addition, the samples were weighed on two different scales and both provided the same masses for each sample before and after deposition and ensures there is no calibration error in them. It must be noted that the mass increase for some samples is fairly small and a deviation of 0.2 mg in the deposit mass already results in significant changes for the CE%, therefore some values that are >100% still fall within 100%-range when 0.2 mg is subtracted from their measured value. In addition, the amount of samples with a CE% >100% is larger for the deposits obtained from highly concentration copper solution (1.25 M). A more inclusive approach to determine the current efficiency is possible through in-situ electrochemical quartz crystal microbalance (EQCM).

4.2.3. Electrodeposition of Cu onto carbon electrodes

The results and discussion on the electrodeposition of Cu onto porous 3D scaffolds are presented in the following sections. Firstly, Cu electrodeposition from acetonitrile is presented. Secondly, the capacitance measurements of thermally treated carbon electrodes are presented and are followed by the results and discussion on Cu electrodeposition from aqueous solutions.

4.2.3.1. Electrodeposition of Cu onto ELAT hydrophilic from acetonitrile

Electrodeposition of Cu in MeCN was investigated to test the hypothesis of a fully wetting, low surface tension solvent. Cu was electrodeposited onto ELAT hydrophilic at -0.85 V with a charge limit of 8 C. The SEM results are shown in Figure 25. The woven structure of the carbon electrode is seen and there are only a few small particles visible on the fibers. It is suggested that these particles are dust due to their morphology. EDS was performed to validate the nature of the particles and the elemental map is presented in Figure 26.

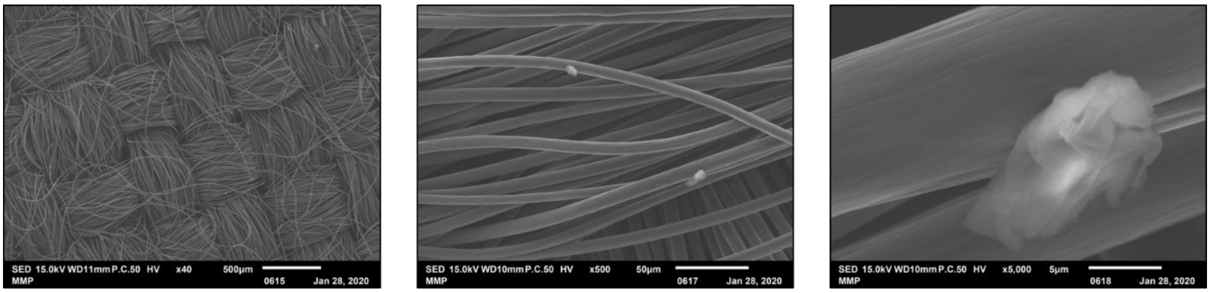

Figure 25 - SEM images of Cu from ACN onto ELAT hydrophilic with a charge limit of 8 C. Only a few small spots are visible.

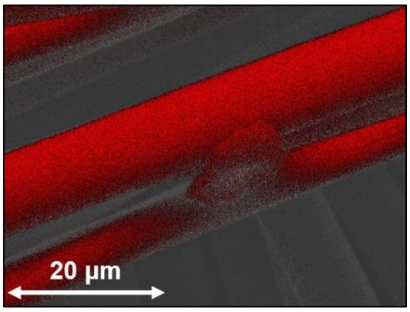

Figure 26 - EDS of Cu from ACN onto ELAT hydrophilic with a charge limit of 8 C. Carbon is marked red.

It appears that the particle is made out of the same material as the fibers and no Cu content is measured. This indicates that the particle is either a dust particle or a small bit of fiber.

The deposition time was increased to figure out if a deposit could be obtained (with t_{dep} = 20, 30 and 58 minutes). Only for the samples of 30 and 58 minutes, a deposit was obtained and the SEM images for t_{dep} = 30 min are presented in Figure 27. However, it was found to be very difficult to reproduce the results.

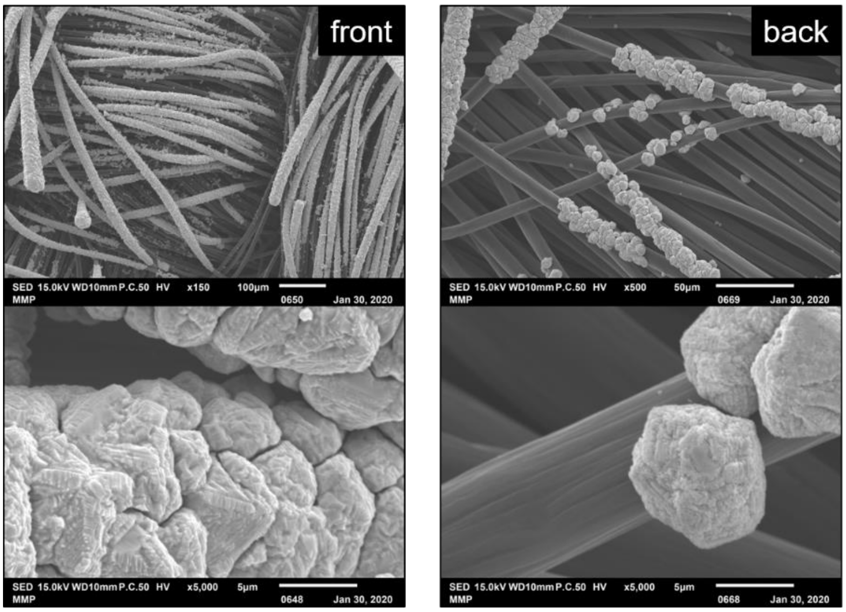

Figure 27 – SEM images of the front and back side of Cu on ELAT hydrophilic with t_{dep} = 30 min deposited from acetonitrile solution.

Both the front and the back of the electrode are investigated, and it can clearly be seen that the back obtains less deposit compared to the front of the electrode. Diffusion towards the backside of the electrode is not promoted because the setup contains only a CE facing towards the front of the electrode. An approach of interest is the use of two CE which are located on both sides of the WE, or use a cylindrical CE that wraps around the WE, or use a rotating WE to create a more evenly distributed current.

Also, it is observed in Figure 27 that the outer fibers are covered with more deposit compared to the inner fibers of the electrode. Cross sectioning could be performed to see validate these findings. Further research must be conducted to improve the homogeneity, and pulse reverse plating might be a method of interest [35], [48]. By alternating anodic and cathodic pulses, the deposit of the outer layer is reduced during the cathodic pulse and diffusion of copper ions towards the bulk of the electrode becomes easier during the anodic pulse.

In Figure 28, the SEM images are shown of the front and the back of Cu on ELAT hydrophilic with a deposition time of 58 minutes. Similar observations are made compared to t_{dep} = 30 min, where the inner fibers are now visibly more covered compared to the use an aqueous solution (section 6.2.2.). However, the results for the back of the electrode appear to be deviating from low coverage to high coverage. Again, this can be attributed to the current distribution that results in less deposit on the back of the electrode.

It was expected that the wetting of the electrode improves when MeCN is used as a solvent instead of water. However, if we compare these results with the results of sections 4.2.3.3. and 4.2.3.4. no significant improvement is observed in the homogeneity of the deposit. In addition, the reproducibility of the fabricated Cu doped carbon electrodes is low and therefore less attractive than electrodeposition in aqueous media.

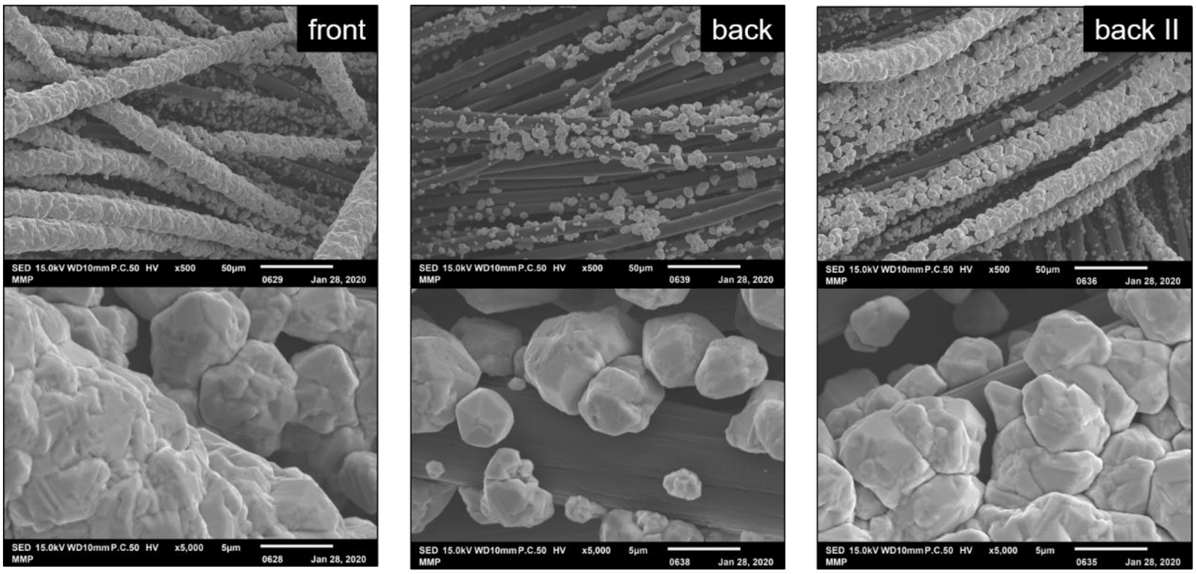

Figure 28 - SEM images of the front and back side of Cu onto ELAT hydrophilic with t_{dep} = 58 min deposited from acetonitrile solution.

4.2.3.2. Capacitance of pristine and treated carbon electrodes (aq.)

Porous materials are known for their high surface area. Therefore, the geometrical surface area of a porous electrode will be smaller than the real surface area if the contact between the electrolyte solution and the porous electrode is high. When determining the roughness factor, one can derive whether the wettability of the porous electrode has increased. Since the electrodes are porous a high roughness factor is expected when the liquid reaches all surface area of the electrode. The experiments performed in an aqueous media showed high wettability for the porous electrode when it has an increased roughness factor.

The heat treatment induced the oxidation of the carbon material, creating functional groups that improve the interaction with aqueous media. It is expected that the capacitive current increases for thermally treated carbon electrodes compared to no heat treatment. Full wetting is desired to assure full contact between the electrode and the solution and therefore enabling electrodeposition of metals in the bulk of the electrode.

The wettability was investigated when immersing the carbon electrodes into the aqueous solution and a visual example of the wetting of untreated and treated Sigracet 39AA is presented in Figure 29. Untreated Sigracet 39AA showed unproper wetting of the electrode since small air pockets are present on the surface of the electrode. For treated, the wetting seemed to be improved since there are barely any air pockets present on the electrode.

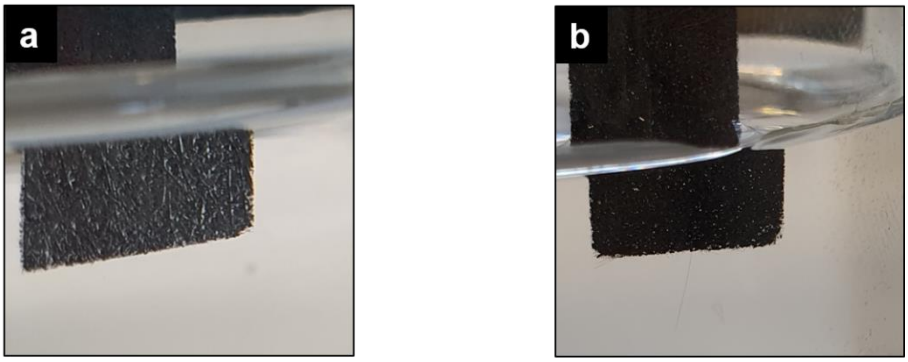

Figure 29 - Sigracet 39AA is shown. a) untreated Sigracet 39AA shows unproper wetting of the electrode (small air pockets are present). b) treated Sigracet 39AA shows a fully wetted outer surface.

The capacitance of the carbon electrodes was used to estimate the electrochemical double layer capacitance (EDLC) and the electrochemically active surface area (ECSA) of the electrode. The results are presented in Table 3.

Table 3 - The electrode double layer capacitance (EDLC) and electrochemically active surface area (ECSA) are presented for both treated and untreated carbon electrode materials.

	Untreated		**Treated**	
Material	**EDLC (µF)**	**ECSA (cm^2)**	**EDLC (µF)**	**ECSA (cm^2)**
AvCarb felt	29 ± 20	$7.6\ 10^{-1} \pm 6.2\ 10^{-1}$	$2.5\ 10^{3} \pm 41$	97 ± 4.9
Sigracet 39AA	7.1 ± 0.4	$1.6\ 10^{-1} \pm 7.0\ 10^{-2}$	$4.0\ 10^{4} \pm 5.4\ 10^{3}$*	$8.9\ 10^{2} \pm 85$*
ELAT Hydrophilic	$5.2 \pm 2.2\ 10^{-2}$	$8.9\ 10^{-3} \pm 3.8\ 10^{-5}$	$1.1\ 10^{3} \pm 31$	$2.0 \pm 2.5\ 10^{-2}$
Freudenberg H23	25 ± 12	$2.4\ 10^{-2} \pm 1.8\ 10^{-2}$	$9.5\ 10^{3} \pm 2.5\ 10^{3}$	23 ± 5.1
Toray Paper	10 ± 3.0	$1.0\ 10^{-2} \pm 2.6\ 10^{-3}$	$1.4\ 10^{2} \pm 1.1\ 10^{2}$	$1.0\ 10^{-1} \pm 7.0\ 10^{-2}$

For treated Sigracet 39 AA, the capacitance curve showed an oval shape. The experiment was repeated, however, the thermal treatment time was increased from 2 hours to 30 hours. In this case, the increase in EDLC and ECSA is significant. It relates to the longer thermal treatment time that increases the oxides and thus increases the amount of functional groups on the electrode surface. A better wetting is therefore expected. In the other cases, the EDLC and ECSA improved after the thermal treatment. This also relates to an improved interaction between the electrode and the solvent due to the increase of functional groups.

4.2.3.3. Pulsed electrodeposition of Cu onto ELAT hydrophilic (aq.)

Pulsed electrodeposition was performed with a cycle of 10 ms for a total deposition time of 90 seconds. The on- and off-time was varied as following: t_{on} = 1 ms and t_{off} = 9 ms, t_{on} = 2 ms and t_{off} = 8 ms, t_{on} = 4 ms and t_{off} = 6 ms. The different t_{on} times are also given in Figure 30. The SEM images of the PED of copper onto ELAT hydrophilic are presented in Figure 31. The experiment was potential controlled at -0.3 V during t_{on} and 0.0 V during t_{off}.

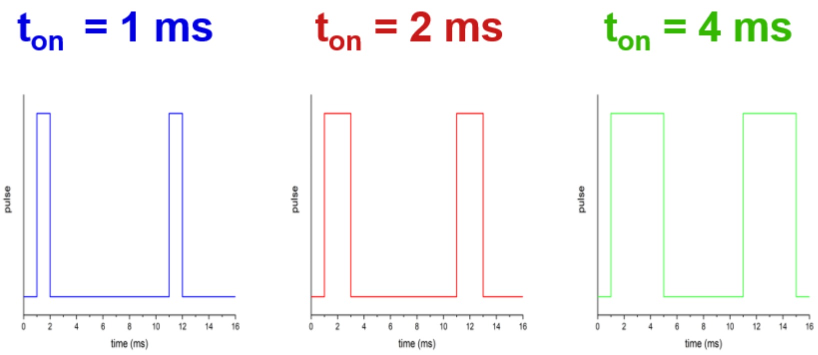

Figure 30 – The varying t_{on} and t_{off} values for the PED of Cu onto ELAT hydrophilic are schematically shown. For each the total period of pulse and off time is 10 ms.

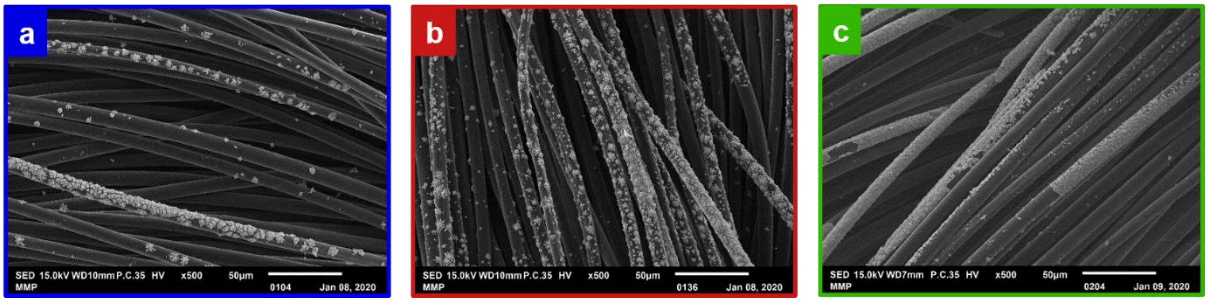

Figure 31 - PED of Cu onto ELAT hydrophilic without stirring for different on times: a) 1 ms, b) 2 ms, and c) 4 ms. The total period of the pulses are constant (10 ms).

The on times for Figure 31 are increasing from left to right, from 1 ms, 2 ms, to 4 ms at a fixed period of 10 ms. The coverage of the fibers appears to increase for a longer applied reduction potential (i.e. t_{on} increases). This relates to an increase in current that passes through the substrate and therefore results in a higher total charge that goes through the sample. This is supported by Faraday's law of electrolysis (eq. (13)), which states that the amount of mass deposited increases with increasing total charge passed through the sample. The deposition of copper particles mainly occurred at the top fibers of the electrode and thus diffusion towards the bulk was not yet attained.

Diffusion of Cu^{2+} ions towards the inner fibers is expected to improve when the solution is stirred. Stirring enhances the mass transport of Cu^{2+} ions towards the electrode through convection. A stirring rate of 400 rpm is introduced to the PED. In Figure 32, the SEM images are presented for the different on times, increasing from left to right.

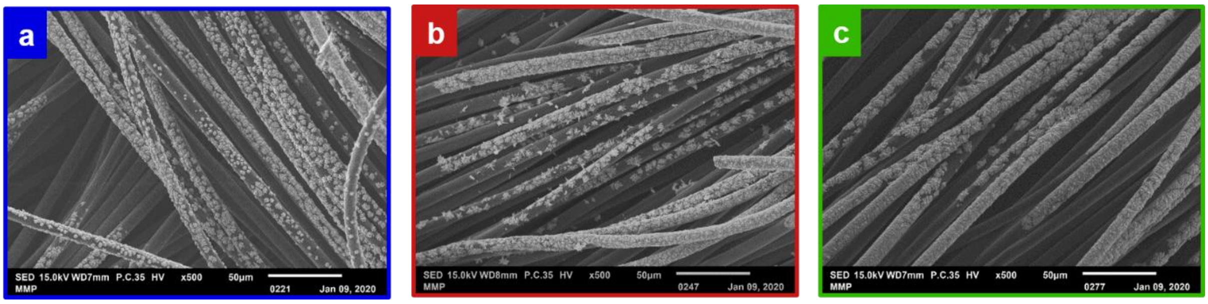

Figure 32 - PED of Cu onto ELAT hydrophilic with a stirring rate of 400 rpm for different t_{on}: a) 1 ms, b) 2 ms, and c) 4 ms. The total period of the pulses are constant (10 ms).

The coverage appears to increase for a longer t_{on} which is similar to the PED without stirring. This is due to a larger total charge during deposition, presumably.

When comparing Figure 31 with Figure 32 the overall coverage improves when stirring the solution. A stirring rate higher than 400 rpm could not be operated due to the magnetic stirrer hitting the frame. However, it appears for both with stirring and without stirring that the fibers in the bulk are still not covered. The deposition preferentially occurs at the outer fibers. Bulk electrodeposition is not promoted through stirring, because diffusion towards the bulk does not occur. The main purpose of stirring is creating a homogenous mixture. This mixing is easier in the bulk electrolyte compared to the electrolyte in the pores.

4.2.3.4. Pulsed electrodeposition of Cu onto Freudenberg H23 (aq.)

The next step was introducing a very short anodic pulse (positive current) of 2 ms to discharge the capacitance of the barrier layer and to interrupt the electric field at the deposition interface, as seen in a study from K. Nielsch et al [47]. This method is referred to as reverse pulse electrodeposition and a schematic representation is presented in Figure 21, section 4.2.2..These experiments were performed in a solution of 1.25 M $CuSO_4$ and 0.5 M H_2SO_4. The cathodic pulse was varied to study the effect of migration during electrodeposition. The off time was varied to study the effects of ion concentration recovery near the electrode and the diffusivity of the ions towards the electrode. In all experiments, the anodic pulse was fixed at 2 ms, a total of 500 cycles were run, and the current applied was ±100 mA.

The off time was varied for each cathodic pulse (t_c = 0.05 s, 0.1 s, and 0.5 s). In Figure 33, the potential vs. time curves for the different off times (t_{off} = 0.1 s, 1.0 s, and 5.0 s) are presented. A fixed cathodic and anodic pulse of ±100 mA was taken for 0.05 s and 2 ms, respectively. The curve (red) for t_{off} = 1.0 s shows a less negative potential value compared to the other t_{off}. In the SEM images, it is also observed that for t_{off} = 1.0 s less deposit is observed on the electrode. This is supported by the less negative potential value of about -0.175 V compared to the values of t_{off} = 0.1 s and 5.0 s that are -0.225 V and -0.232 V, respectively. An explanation for the less negative potential for t_{off} = 1.0 s was difficult to be determined. For the SEM images with t_{off} = 0.1 s and 1.0 s, deposition also occurred on the fibers that are lie further into the electrode. To validate how the far the copper ions diffused into the electrode to create a deposit, a cross section should be prepared. However, we found this to be a limitation since it is difficult to create a clean cut of the electrode without affecting the fibers. A more brittle electrode material with similar pore sizes is preferably desired.

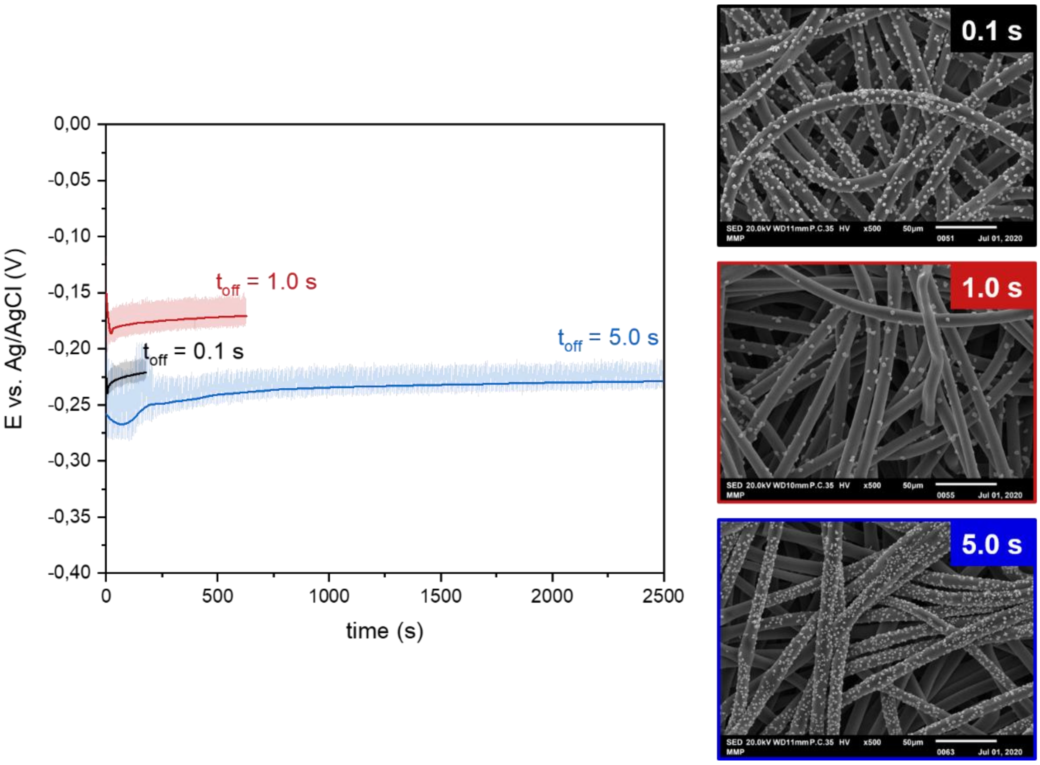

Figure 33 - On the left, the potential vs. time curve is presented for the different off times (t_{off} = 0.1 s, 1.0 s, and 5.0 s) for a fixed cathodic and anodic pulse of ±100 mA for 0.05 s and 2 ms, respectively. On the right, the corresponding SEM images are presented that show the coverage of Cu onto Freudenberg H23.

In spite of having a cross sectional cut, a rough analysis of the penetration depth is proposed. The electrode material has a thickness of 210 µm. The fibers are 10 µm in diameter and the maximum deposition depth that is reached for each off time is estimated to be the fourth layer. The maximum deposition depth is therefore around 40 µm, which represents about 19% of the electrode thickness. Assuming that only diffusion took place during t_{off}, the mean distance travelled can be estimated based on the diffusion coefficient of Cu and t_{off}. For the shortest time (t_{off} = 0.1) and the calculated diffusion coefficient in section 4.2 ($D = 5.32 \times 10^{-6}$ cm^2 s^{-1}), the mean distance travelled is about 10 µm. The mean distance increases to 33 and 73 µm for t_{off} = 1.0 and 5.0 s, respectively. Comparing the calculations to the estimated maximum penetration depth, it is expected that the copper ions possibly penetrate deeper into the electrode for longer off times. In practice, there seems to be a limiting penetration depth that might be caused by improper wetting of the electrode and therefore prevents the electrodeposition of copper in the bulk.

In Figure 34, the potential vs. time curves for the different off times (t_{off} = 0.1 s, 1.0 s, and 5.0 s) are presented. A fixed cathodic and anodic pulse of ±100 mA was taken for 0.1 s and 2 ms, respectively. The potentials appear to be closer together in value for t_c = 0.1 s compared to the values of t_c = 0.05 s (Figure 33). The SEM images show mainly deposition on the top fibers of the electrode and the coverage appears to increase for longer off times. This suggests that the crystals have time to grow and that is also supported by the morphology of the crystal. For increasing t_{off} the crystal structure appears to be less round and more spread.

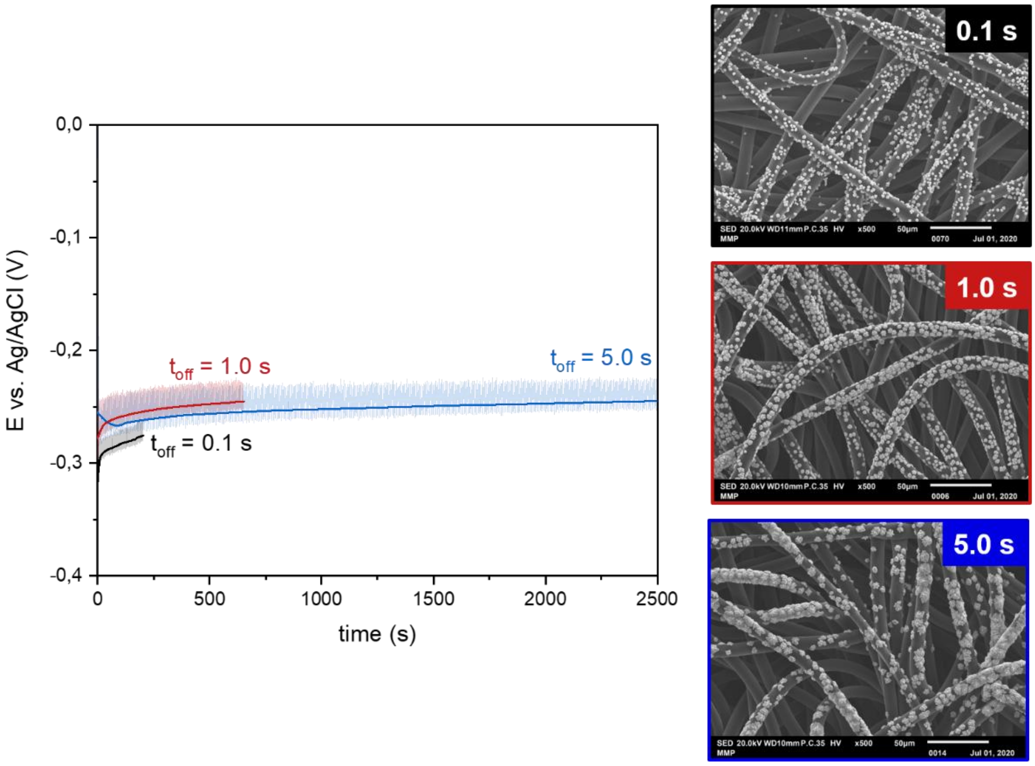

Figure 34 - On the left, the potential vs. time curve is presented for the different off times (t_{off} = 0.1 s, 1.0 s, and 5.0 s) for a fixed cathodic and anodic pulse of ±100 mA for 0.1 s and 2 ms, respectively. On the right, the corresponding SEM images are presented that show the coverage of Cu onto Freudenberg H23.

In Figure 35, the potential vs. time curves for the different off times (t_{off} = 0.1 s, 1.0 s, and 5.0 s) are presented. A fixed cathodic and anodic pulse of ±100 mA was taken for 0.5 s and 2 ms, respectively. A decrease towards more negative values is observed for the deposition potential when increasing the off time. The deposits shown in the SEM images show similar morphology for t_{off} = 0.1 s and 1.0 s resulting in fairly round particles, whereas the morphology of t_{off} = 0.5 s appears to have grown crystals. In addition, both the top and back fibers appear to have Cu deposit. As mentioned before, a cross section is necessary to determine the amount of diffusion of Cu^{2+} ions towards the bulk of the electrode.

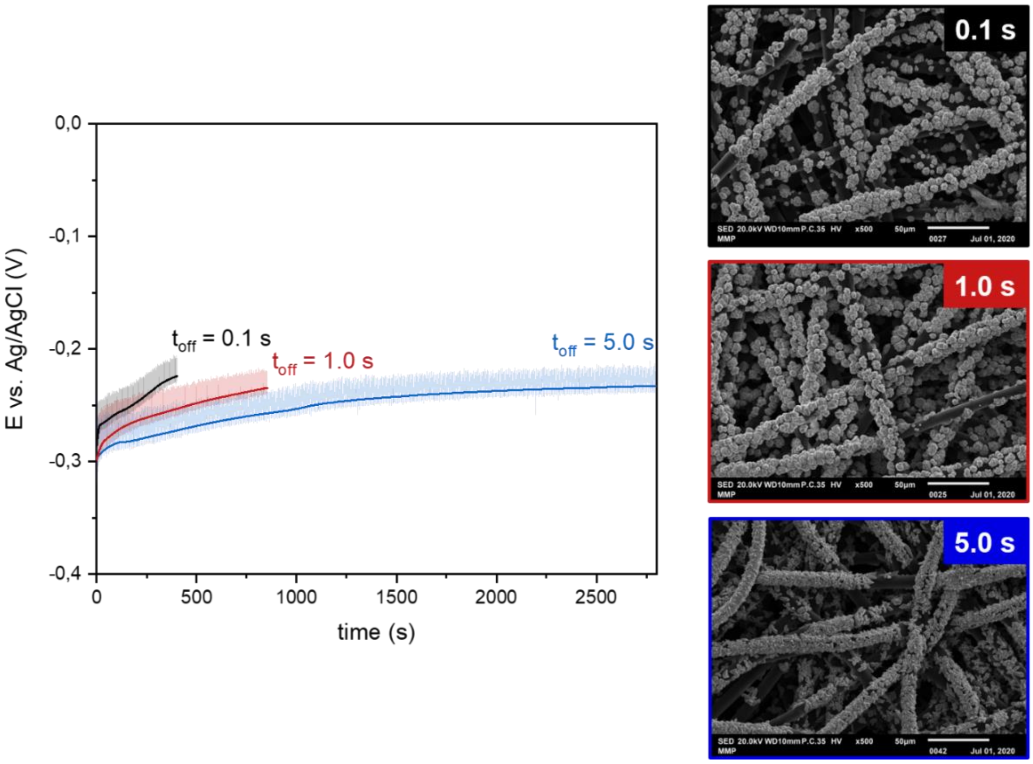

Figure 35 - On the left, the potential vs. time curve is presented for the different off times (toff = 0.1 s, 1.0 s, and 5.0 s) for a fixed cathodic and anodic pulse of ±100 mA for 0.5 s and 2 ms, respectively. On the right, the corresponding SEM images are presented that show the coverage of Cu onto Freudenberg H23.

Comparing the deposits of Figure 33, Figure 34, and Figure 35 it appears that an increase in deposit is found, which is expected for a longer cathodic pulse. Deposition mainly occurs on the outer fibers of the electrode, however, to the longest cathodic pulse (t_c = 0.5 s), deposit clearly appears on the inner fibers as well. This suggests that a shorter cathodic pulse is not sufficient to obtain deposition in the inner fibers. In addition, the particle size increases for longer t_c. This is attributed to the favorable interaction between Cu^{2+} and Cu as a substrate vs Cu^{2+} and carbon fibers as a substrate. This is of interest for the field of electrocatalysis to tune the particle size of the electrocatalyst.

Chapter 5 - Electrodeposition of Nickel

5.1 Introduction

Nickel deposition is widely used as a coating material for decorative and functional applications [57], [58]. The Watts bath is commonly used for decorative processes whereas nickel sulfamate solutions are more suitable for functional plating. The Watts bath consists of nickel sulfate, nickel chloride and boric acid and is operated at elevated temperatures with a pH of 4.0 and a soluble nickel anode. Additives such as organic and metallic compounds improve the deposit, making it brighter and level the deposit. Nickel sulfamate baths have a higher electroplating speed and it is easier to obtain thick deposits with less internal tensile stress [59].

One component that is used in both Watts baths and nickel sulfamate solutions is boric acid. The role of boric acid has been discussed widely in literature, and the stated effects in literature are: 1) pH buffering agent, 2) catalyst for Ni electrodeposition to lower the overpotential, 3) suppression of HER, 4) accelerating deposition growth rates, and 5) reduction of passivation of the deposited layer [59]–[61]. In recent research, it was found that the tensile strength of the Ni deposit improves for higher the concentrations of boric acid [62].

The adsorption of Ni^{2+} ions is generally described as follows [63]:

$$Ni^{2+} + X^{-} \rightarrow NiX^{+} \quad (23)$$

$$NiX^{+} + e^{-} \rightarrow NiX_{ads} \quad (24)$$

$$NiX_{ads} + e^{-} \rightarrow Ni + X^{-} \quad (25)$$

Where X^- indicates an anion that is assumed to be OH^-, Cl^- or SO_4^{2-}. In the Watts bath containing both boric acid and a chloride salt, it is assumed that Cl^- is the anion. In the absence of boric acid, the nickel monohydroxide ion $NiOH^+$ is formed according to some studies [63].

A challenge in nickel electrodeposition originates from its reduction potential being close to the reduction potential of water, causing hydrogen evolution to occur. It is stated in literature that H^+ is reduced to H_{ads} and the formed H_{ads} bonds to the surface and reacts with Ni^{2+} ions, causing formation of the insoluble $Ni(OH)_2$ that acts as a passivation layer [61]. This inhibits the formation of Ni. Other literature mentions the formation of hydrogen bubbles on the cathode surface that stick onto the surface and therefore causing inhibition of nickel deposition. To improve the cathodic efficiency, (anionic) surfactants can be added like SLS (sodium lauryl sulfate) to aid the release of hydrogen bubbles that are left on the surface which has been used in the electrodeposition of NiCu bimetal onto carbon paper [64]. Another role of boric acid that has been investigated in these studies is the effect on the pH in vicinity of the substrate. It was found that the pH near the substrate surface is maintained at the value of the bulk due to the presence of boric acid [59], [61].

The Watts bath remains a base for other studies on Ni electrodeposition. Throughout the years, scientists have been exploring a variety of different parameters and bath compositions including the use of different aqueous electrolytes and their role on the thickness of the formed deposit, the grain size, lattice strain, stress, and hardness [65]. Also modified Watts baths containing saccharin as a grain refining agent were studied at different temperatures and applied current densities [66] and varying stirring rates [67] to investigate their role on mechanical properties. A more recent study focused on the electrodeposition of Ni from a sulfamate bath containing different concentrations of Ni sulfamate, boric acid, and a varying applied current density better understand the fundamental mechanisms that relate stress to growth rate, grain size, and electrolyte concentrations [62]. Another recent study investigates the possibilities of fabricating a nanocrystalline Ni film with a grain size gradient [68]. Reasons to investigate nanocrystalline Ni with a grain size gradient are improved strength and ductility [69], [70].

One study focused on the quantitative measurement and the analysis of HER using EQCM, to observe the co-deposition of Ni and hydrogen during Ni deposition [71]. EQCM provides an in-situ measurement of electrode mass at the nanogram level during EC reactions. The effect of HER on the electrodeposition of nickel was studied through the hydrogen permeation technique. This technique provides information about the adsorbed hydrogen during electrodeposition. A summation is presented of Ni deposition, hydrogen adsorption, and hydrogen evolution that accounts for the total charge of the electrodeposition. A scheme is proposed to estimate the relation between Ni and hydrogen reduction and the total charge required. In addition, the effect of boric acid is studied and it was found that the formation of nickel hydroxide occurs in the absence of boric acid and is confirmed through EQCM measurements.

Other studies focused on the use of other solutions and additives to improve the deposit. Among these, alcoholic solutions were investigated to study the effect of solvent on the morphology of the deposit [72]. The addition of quaternary ammonium sulfate salts to the Watts bath was studied and the obtained Ni deposit showed an improved corrosion resistance [73]. Deep eutectic solvents were investigated and resulted in different morphologies of electrodeposited Ni [74], [75]. Ionic liquids were studied, because these liquids inhibit HER and other chemical side reactions prone in aqueous media, increase the potential window (range of stability), improve the solubility of metal salts, improve the conductivity compared to non-aqueous solvents, and due to their low vapor pressures are an adequate candidate to perform ED at a range of temperatures [76]–[79]. However, the disadvantages are that ionic liquids are quite expensive compared to aqueous solutions and often have a higher viscosity.

Hydrogen evolution remains a challenge in electrodeposition of Ni from aqueous solutions, especially at lower concentrations and at higher current densities. A study by K. Nielsch et al explored the method of pulsed electrodeposition to obtain a uniform Ni deposit into ordered alumina pores [47]. A thoroughly review on this paper is presented in section 4.1.1..

Nickel is a stable metal that can be used as a porous electrode material and is commercially available. However, studying the versatile technique of electrodeposition is assumed to be a novel way to increase the ECSA of an electrode. The ECSA can for example be further increased by electrodeposition of particles onto a porous scaffold. Recently, Yu, H., Quan, T., Mei, S. et al. demonstrated the electrodeposition of Ni nanodots onto Ni foam for the fabrication of a high-performance water splitting electrode [30]. The fabricated electrodes showed superior performance during HER and oxygen evolution reaction (OER) and proved to be durable for at least 20 hours without potential decay for a fixed current density. This makes the electrode material also interesting for RFBs, where stability is important and a larger surface area improves the performance. The porous electrodes are fabricated through electrodeposition of nickel nanodot onto nickel foam from nickel nitrate ($Ni(NO_3)_2$) in N_2-saturated acetonitrile (ACN). Subsequently, the sample is oxidized to passivate the porous structure. The use of acetonitrile prevented the formation of hydrogen. Acetonitrile was investigated due to its acclaimed higher thermodynamic stability even though their potential windows are similar [80].

Yan-Li Zhu, Yukari Kozuma et al. showed that Ni is able to form a complex with acetonitrile [80], however in this case Ni bis(trifluoromethylsulfonyl)amide ($Ni(TFSA)_2$) is used instead of hydrated nickel nitrate. Preliminary work was carried out and addressed the electrochemical behavior of Ni^{2+}/Ni in an amide-type room-temperature ionic liquid [76]. They reported that Ni^{2+} can be reduced to Ni from a hydrophobic ionic liquid (1-butyl-1-methylpyrrolidinium bis(trifluoromethylsulfonyl)amide) and that the electrocrystallization of Ni involved instant 3D growth (Volmer-Weber) under diffusion control. In the case of $Ni(TFSA)_2$/BMPTFSA with ACN, a positive shift was observed in CV measurements and suggested a decrease in the overpotential of Ni^{2+} reduction. The donor property of ACN is higher than $TFSA^-$, and therefore the thermodynamic stability of $[Ni(ACN)_6]^{2+}$ is higher than $[Ni(TFSA)_3]^-$. The charge of both complexes plays a crucial role in the compensation of the negatively charged substrate. $[Ni(ACN)_6]^{2+}$ is able to access the electrode surface whereas $[Ni(TFSA)_3]^-$ is hindered.

To sum up, Ni electrodeposition has proven to be challenging due to the generation of hydrogen bubbles at its low reduction potential. Methods to eliminate the consequences of HER have been studied and several procedures have been developed to decrease the formation of hydrogen bubbles that affects the morphology of the Ni deposit. The procedures include the use of additives, applying an alternating current (through pulsed electrodeposition) and performing the electrodeposition in organic media.

Based on the literature provided above, we hypothesize that pulsed electrodeposition results in a high current efficiency for Ni deposition onto 2D substrates due to the introduction of an off time to reduce the consequences of HER and to replenish the Ni^{2+} concentration at the surface.

5.2 Results and discussion

5.2.1. Ni onto graphite foil

After electrodeposition, bright Ni deposits are obtained. This suggests that the deposit is very conformal and the formation of nickel oxides or hydroxides did not occur.

In Figure 36a, the potential (during the cathodic pulse) versus time curves are presented for each different cathodic pulse time. It is observed that during the cathodic pulse, the potential E drops during this period. For increasing t_c the magnitude of the potential drop decays faster and also finishes in a smaller potential difference in each pulse. This is due to the longer deposition period and therefore the concentration near the surface is faster depleted, resulting in more negative potentials during deposition.

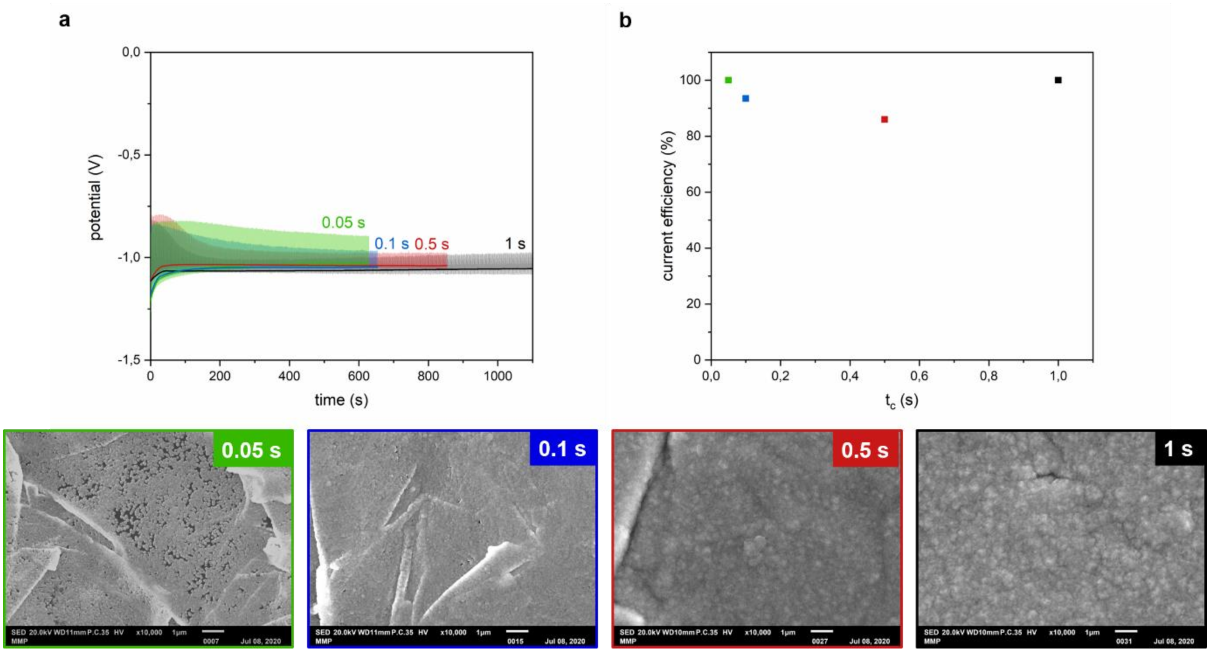

Figure 36 - a) The potential vs. time curve is presented for the different cathodic pulse times. b) the current efficiency vs. cathodic pulse time is presented. Below, the SEM images are presented at a magnification of 10,000 x of the Ni deposit onto graphite foil at different cathodic pulse times.

In Figure 36b, the current efficiencies for each deposit at different cathodic pulse times are presented. The current efficiencies show that Ni is mainly deposited (CE% >86%) onto the graphite foil and HER evolution is suppressed. For highly concentration solutions CE% of >100% are found. An explanation for this behavior is presented in section 4.2.2..

In addition, the SEM images are presented in Figure 36. For t_c = 0.05 s, the nickel deposit does not fully cover the graphite foil. Also, cuts and uneven slants are visible in the deposit layer. This is a result of the morphology of graphite foil that already has an uneven surface structure (roughness factor of ~ 30). For t_c = 0.1 s, these cuts and slants are also visible, however, the coverage has improved compared to t_c = 0.05s. The longer cathodic pulses (0.5 and 1 s), have both a high coverage and some grain boundaries are visible. This relates to the effect of the pulse time on the morphology. The affinity for Ni interactions increases from Ni-solution, to Ni-graphite foil, to Ni-Ni. In the case of PED, grain boundaries result from the island growth that is favorable because of the preferred Ni-Ni interaction. However, only a short current is applied and therefore the nucleation points are located randomly and there is a lot of uncovered graphite foil present. If the deposited Ni is out of range, Ni-solution and Ni-graphite foil interactions are the only competitors. This results in a lot of small nucleation island over the substrate and thus some visible grain boundaries. In Figure 37, it can be seen that there is some pitting present in each sample, indicating that HER occurred during deposition.

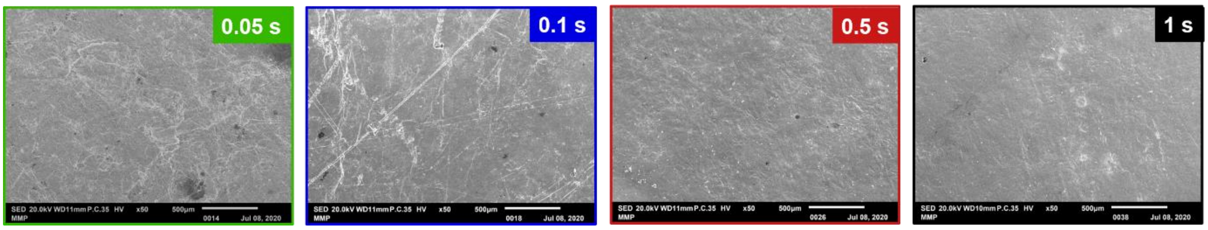

Figure 37 - The SEM images of Ni onto graphite foil at different cathodic pulse times (presented in the upper right corner of each image).

We hypothesized that PED is able to reduce HER and that a conformal coating can be formed. It was observed that nucleation overpotential is decreased through PED. In these conditions, island growth is preferentially under kinetic control, resulting in a conformal deposit. This was validated through the bright Ni deposit that was obtained, however, there were still some grain boundaries and pitting visible at the microscale. The CE% of each t_c is larger than 86% and this indicates that HER is still present. This is supported by the pitting that is observed.

Chapter 6 - Electrodeposition of Ni-Cu alloy

6.1 Introduction

The co-deposition of Ni-Cu alloys has been of interest for a long time. It has been widely of interest due to their high tensile strength, malleability and ductility as well as their unique magnetic properties, high corrosion resistance in harsh environments and good catalytic properties. Ni and Cu are known for their similar lattice parameters (3.499 and 3.597 Å, respectively) and both are face-centered cubic (fcc). They form a solid solution across the whole compositional range and therefore assure maximum flexibility in tailoring the properties over a wide range. Adding to this, it is possible to predict the composition based on the deposition kinetics of the individual metals. This is due to their independent reduction potentials that are shown in Figure 38 and start at -0.143 V and -0.447 V vs. Ag/AgCl for Cu and Ni, respectively [81].

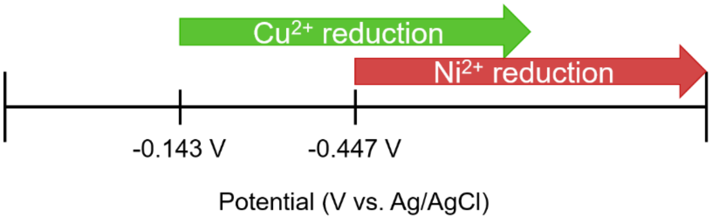

Figure 38 - The reduction potentials are shown for Cu^{2+} and Ni^{2+}.

A study conducted in 1998 found that Ni-Cu co-deposition only occurs in a small potential window of -0.955 V to -1.155 V vs Ag/AgCl, where the side effects are not so prominent [82]. In 1995, others report the co-deposition of Ni and Cu within a larger potential range of -0.700 V to -1.300 V [51]. Through ex-situ XPS analysis the coulombic/current efficiency was determined and plotted vs. the deposition potential. The current efficiency reached a minimum where Cu deposition becomes mass transfer limited and where the Ni deposition is still low/slow (-1.000 V vs. Ag/AgCl). Here, other species such as O_2 and protons are reduced and evoke competition. Side reactions that might evolve are HER since an extreme reduction value is needed to deposit the alloy. The HER elevates the pH in the vicinity of the electrode, causing the formation of oxides/hydroxides. This leads to the passivation of the substrate and therefore no longer metallic ions can be reduced on the surface. Hence, the co-deposition of Ni-Cu alloys appears to be a challenging task.

A difference in the reduction potential between two elements in a homogeneous alloy can lead to selective etching of the more active component and leaves a porous structure behind. This process is known as dealloying and might be of interest in the fabrication of porous metallic electrodes. In 2004, a study was conducted by Searson et al into the fabrication of nanoporous nickel by electrochemical dealloying [81]. Here, they reported a method to dealloy copper from a NiCu film that is au contraire since nickel is in this case more active than copper. A nickel sulfamate bath was used and resulted in the formation of a passivating oxide layer, therefore allowing the selective etching of copper. The pore size of the dealloyed structure depends on the alloy composition, resulting in a method that is easy tailored by altering the composition of the deposit. This composition is changed by altering the reduction potentials in the range between the reduction potentials of Ni and Cu.

We hypothesize that through electrodeposition of NiCu alloy film onto Ni foam and subsequently dealloying copper from Ni-Cu alloy films, an electrode with larger surface area can be fabricated, improving the electrochemical properties of the electrode.

6.2 Results and discussion

6.2.1. Deposition of NiCu onto nickel foil

In Figure 39 the SEM images are shown for different deposition potentials with a fixed total charge of 8 C. The deposition solution contained 0.8 M $Ni(H_2NSO_3)_2$ + 0.05 M $CuSO_4$ + 0.4 M H_3BO_3. It appears that for more negative deposition potentials, dendrites become more eminent. EDS is used to characterized the elemental nature of the dendrites and the result is shown in Figure 40, where the sample with deposition potential -1.000 V is presented.

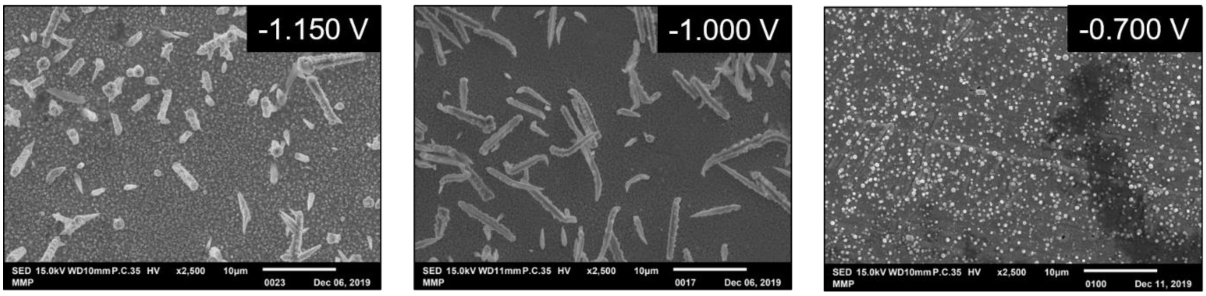

Figure 39 - The SEM images of the $Ni_{0.9}Cu_{0.1}$ deposit onto Ni foil for the different deposition potentials.

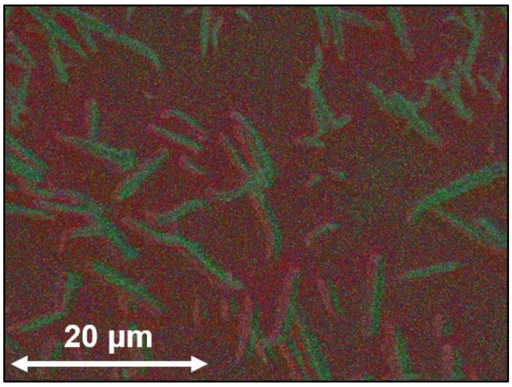

Figure 40 - SEM-EDX image of $Ni_{0.9}Cu_{0.1}$ onto Ni foil at a deposition potential of -1.000 V. The Ni has a red marker and Cu has a green marker.

It appears that the dendrites consists of Cu and that the substrate is a mix of both Ni and Cu. An explanation for the formation of Cu dendrites is given in section 4.2.2.. The large nucleation overpotential for Cu results in island growth that is diffusion controlled and results in the formation of dendrites.

For each deposition potential, the composition of the NiCu film was analyzed using the software of the SEM-EDS. One spot was analyzed per sample and the atomic percentages (at%) and mass percentages (mass%) a presented for each deposition potential in Table 4.

Table 4 - The atomic weight percentages of Ni and Cu onto Ni foil for different deposition potentials with a solution of $Ni_{0.9}Cu_{0.1}$ through SEM-EDX elemental analysis.

E_{dep} [V]	Ni (at%)	Cu (at%)	Ni (mass%)	Cu (mass%)
- 0.700	6.6	93.4	6.1	93.9
- 0.850	71.4	28.6	69.8	30.2
- 1.000	81.1	18.9	79.9	20.1

An increase in Ni content is seen for more negative deposition potentials, which is in accordance with the findings of Searson et al. [81].

The XRD graphs for the NiCu films on nickel foil for different deposition potentials are shown in Figure 41. As a reference, the XRD peaks were also measured for a Cu film and Ni foil. The characteristic peaks of Ni were observed for angles of 44.6 2θ and 51.8 2θ, and for Cu of 43.3 2θ and 50.4 2θ. First, the peaks between 40 2θ and 50 2θ are discussed. For -0.700 V, a flattened peak is observed at 43.6 2θ and for -0.850 V. In addition, for -0.850 V a peak at 43.6 2θ is also observed. At -1.000 V, no peak appears around this value, however a small shoulder is visible around 44.1 2θ. For all deposition potentials, a peak is observed around 44.8 2θ. All the peak values deviate slightly from the pure Ni and Cu films.

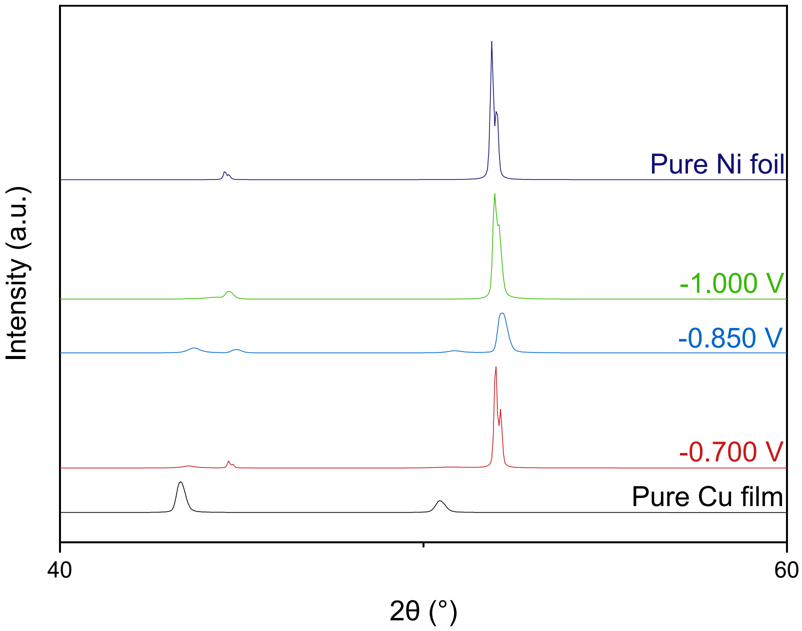

Figure 41 – The XRD data presented for the NiCu films on Ni foil of different deposition potentials. Pure Ni foil and pure Cu film are given as a reference.

The peaks between 50 2θ and 60 2θ show no indication of the presence of copper in the deposits obtained from -0.700 V and -1.000 V. A very small peak is observed for -0.850 V around the 2θ of Cu. In addition, a distinct Ni peak at 52.0 2θ is observed for -0.700 V, -0.850 V, and -1.000 V. Again, small deviations are found for the values of the deposited films compared to the pure Ni and Cu films.

The characterization of NiCu onto Ni foil using EDS and XRD is limited, because the deposited layer is relatively thin, which results in X-rays to reach the substrate creating noise from the Ni foil, which makes it difficult to conclude precisely the ratio of the Ni and Cu on the deposited film. Therefore XRD and EDS is again measured for NiCu deposits on graphite foil to remove the noise. These results are presented in the next section.

6.2.2. Deposition of NiCu onto graphite foil

In Figure 42 the NiCu films on graphite foil are shown for three different deposition potentials. The morphology of the deposit is similar to the deposition of NiCu onto Ni foil. Dendrites are again present for more negative deposition potentials. Figure 43 shows the elemental distribution map for each deposit. In the case of E_{dep} = -0.850 V, dendrites clearly consists of Cu. An explanation on the dendrite formation can be found in section 4.2.2..

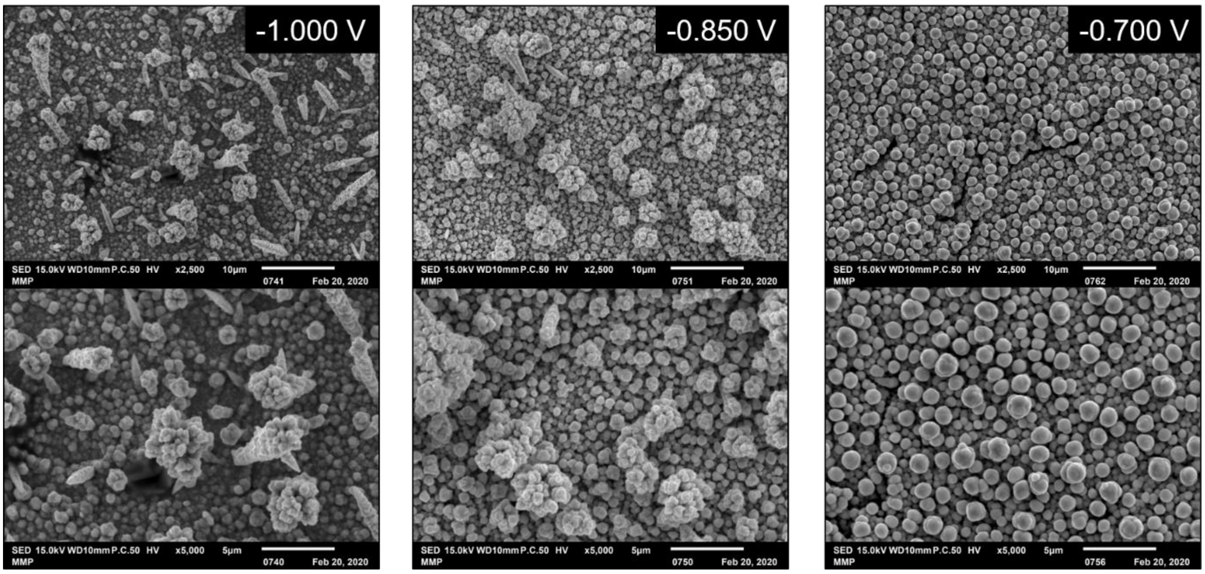

Figure 42 - SEM images of the NiCu film on graphite foil at different deposition potentials for a magnification of 2,500 x (top row) and 5,000 x (bottom row).

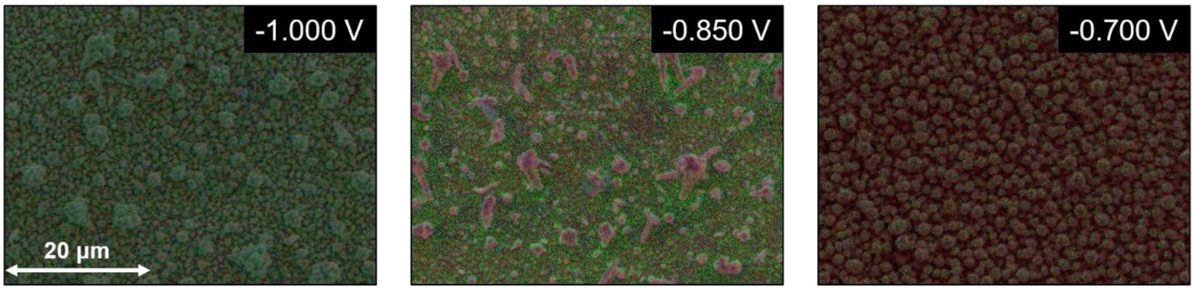

Figure 43 - SEM-EDX images for NiCu film at three different deposition potentials. Nickel (green), copper (red) and oxygen (blue) are marked.

The composition of the NiCu film was analyzed using the software of the SEM-EDS. Two spots were analyzed per sample and the average of the atomic percentages (at%) and mass percentages (mass%) were calculated for each deposition potential and are presented in Table 5.

Table 5 **-** The atomic weight percentages of Ni and Cu onto graphite foil for different deposition potentials with a solution of NiCu through SEM-EDX elemental analysis.

E_{dep} [V]	Ni (at%)	Cu (at%)	C (at%)	Ni (mass%)	Cu (mass%)	C (mass%)
- 0.700	0.0	89.8	10.2	0.0	97.9	2.1
- 1.000	11.1 ± 0.2	79.7 ± 0.5	9.2 ± 0.6	11.2 ± 0.2	86.9 ± 0.1	1.9 ± 0.1
- 1.150	43.9 ± 0.7	41.2 ± 1.9	14.9 ± 2.5	48.0 ± 0.5	48.6 ± 1.1	3.4 ± 0.7

An increase in nickel content is again observed for higher deposition potentials and is in accordance with section 5.2.1. and Searson et al. [81]. The results in Table 5 can be compared with the results of Table 4, and for a deposition potential of -0.700 V, there is no longer Ni present for NiCu film onto graphite foil compared to 6.6 at% of Ni in the NiCu film on Ni foil. The difference in atomic mass and the detection of carbon in the case of NiCu onto graphite foil suggest that the substrate was also measured during the EDX experiment. The acceleration voltage during EDX experiments was 15.0 keV. For higher acceleration voltages, the penetration depth increases [83]. In the case of a smaller film thickness, the X-rays are able to reach the substrate and measure the nature of the substrate as well.

To see if an alloy is obtained, thin film XRD is performed and the graphs for the NiCu films on graphite foil for different deposition potentials are shown in Figure 44a. As a reference, the XRD peaks were also measured for pure Cu and Ni films and are presented as well in Figure 44b. The peaks that are visible in the deposit around 54.6 2θ are characteristic for graphite. In addition, small peaks are measured around 43.4 2θ and 50.6 2θ indicating the presence of single phase copper. The presence of nickel in the deposit is observed only a little for -0.850 V and -1.000 V. It is expected that NiCu forms a homogeneous alloy since it is a solid solution across the whole compositional range. This is characterized by a different diffraction pattern where a new convoluted peak is expected to be found in between the 2θ values of Ni and Cu [84], [85]. The peaks of the electrodeposited NiCu films appear to be very small and makes characterization rather difficult. For the film that was electrodeposited at -1.000 V, a small stretched peak is present in between the 43.4 2θ and 44.6 2θ. This indicates that there is both Cu and Ni present. The formation of NiCu alloy is difficult to confirm, since the peak intensity is low. Further investigation is needed to confirm the formation of an alloy.

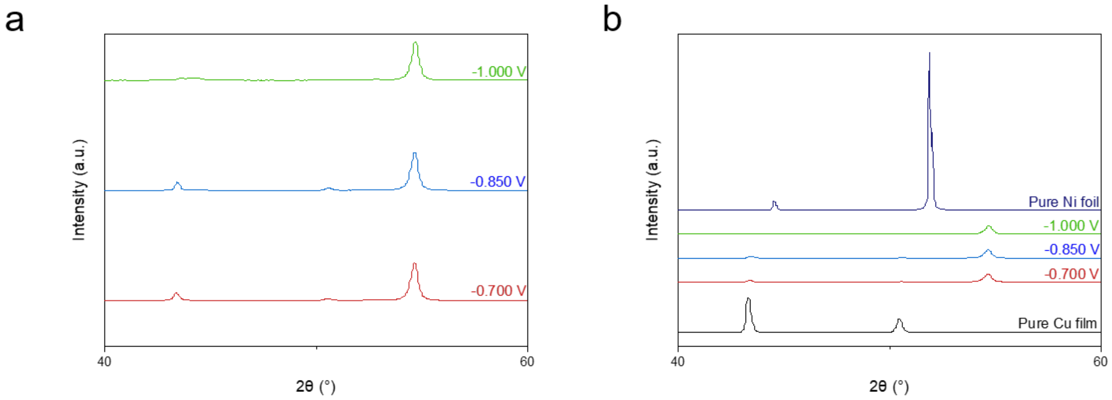

Figure 44 – a) The XRD data presented for the NiCu films on graphite foil. b) The XRD data presented for NiCu films on graphite foil with pure Ni foil and pure Cu film as a reference for the peaks.

A higher intensity peak is needed to determine if an alloy is formed. The amount of deposit or the measuring time can be increased to raise the intensity of the peaks. In addition, deposition of a thicker layer is suggested to prevent the penetration of X-rays to reach the substrate and create a clearer signal.

Chapter 7 - Conclusions and outlook

In this study we have explored electrodeposition of single metals and alloys as a method to fabricate porous electrodes for redox flow batteries. Insight has been gained in the electrodeposition of metals on 2D substrates to better understand the electrochemical process.

- The **wettability of porous carbon electrodes** plays an important role in the electrodeposition. This is particularly relevant in aqueous electrolyte due to the higher surface tension of water. To tackle this issue, an oxidative thermal treatment under air was implemented which resulted in an increased electrochemically active surface area of the electrodes and better accessibility of the electrolyte solution.

- As an alternative approach, I explored the use of **electrodeposition using organic electrolytes** (acetonitrile). It was expected that the wettability of the 3D carbon electrode is better in an organic solvent and thus lead to bulk electrodeposition. These initial experiments feature limitations in obtaining a conformal deposition throughout the porous carbon structure; however, copper was successfully deposited. Future studies should focus on improving the driving force for deposition by, for example, increasing Cu^{2+} concentration, and improving ionic conductivity of the supporting electrolyte.

- **Pulsed electrodeposition of copper** from aqueous electrolytes was investigated systematically. The results suggest that pulsed electrodeposition from low concentration copper solutions is an attractive method to prevent ion depletion in the vicinity of the electrode. For current densities of -50, -100, -150, and -200 mA cm^{-2}, the current efficiency increased from values between 30% and 90% to 100%. The effect of depletion is also eliminated for electrodeposition solutions that contain high copper concentrations and the method is compatible with high current density operation. The application of a relaxation time allows the system to replenish ions which is beneficial for mass transport. The results so far have been promising and pulsed deposition has the potential to achieve electrodeposition of metals throughout a porous electrode. However, future work should target experimental conditions that enable conformal coatings to be achieved. One promising idea would be to employ a flow through electrochemical cell to increase convective transport, and thus improve coating distribution. A better understanding of the fundamentals of electrodeposition on 3D scaffolds is a vital issue for future research. Furthermore, to validate the deposition of copper in the bulk of the electrode, cross sectioning of the electrode is suggested. The current generation of porous electrodes are limited in clean cross sectioning due to their mechanical nature (i.e. flexible), so it is suggested to perform the electrodeposition of copper onto a brittle porous structure with similar pore sizes that is easily fractured or use alternative methods such as ion milling or (cryo-)ultramicrotomy.

- **Electrodeposition of nickel** onto graphite foil was performed with pulse electrodeposition to inform the deposition of the alloy. A fairly conformal coating was obtained and current efficiencies of >86% were found. In addition, pitting due to HER is significantly reduced through pulsed electrodeposition, because the anodic pulse and off time aid the release of hydrogen bubbles. Future work needs to be performed on optimizing the length of the off time and the cathodic and anodic pulses, as well as the applied current density.

- **Electrodeposition of NiCu alloys** was investigated as a preliminary study on the novel approach of fabricating metallic porous electrodes through a bimodal pore distribution. The current study was showed the limitations of NiCu electrodeposition from a copper sulfate and nickel sulfamate bath containing boric acid. The deposition potential of Ni creates a nucleation overpotential for Cu, which results in the formation of diffusion controlled dendrites. Further research will aim at a post treatment after electrodeposition at elevated temperature to promote the interdiffusion of nickel and copper in the NiCu film. In addition, the use of a complexing agent to bring the reduction potentials of Ni and Cu closer together is suggested to obtain an alloy. In conclusion, the electrodeposition conditions are still to be optimized and to be translated to electrodeposition of alloys on 3D porous scaffolds. To achieve this, we are confident that the improved knowledge on single metal pulsed electrodeposition will encourage future work in obtaining a conformal deposition of alloys throughout the 3D scaffold.

Bibliography

[1] D. Spencer, “BP Statistical Review of World Energy Statistical Review of World,” *Ed. BP Stat. Rev. World Energy*, pp. 1–69, 2019.

[2] P. Leung, X. Li, C. Ponce De León, L. Berlouis, C. T. J. Low, and F. C. Walsh, “Progress in redox flow batteries, remaining challenges and their applications in energy storage,” *RSC Adv.*, vol. 2, no. 27, pp. 10125–10156, 2012.

[3] U. Energy Information Administration, “International Energy Outlook 2019,” 2019.

[4] A. De Almeida, P. Fonseca, B. Schlomann, and N. Feilberg, “Characterization of the household electricity consumption in the EU, potential energy savings and specific policy recommendations,” *Energy Build.*, vol. 43, no. 8, pp. 1884–1894, Aug. 2011.

[5] O. Edenhofer *et al.*, “Climate Change 2014 Mitigation of Climate Change Working Group III Contribution to the Fifth Assessment Report of the Intergovernmental Panel on Climate Change Edited by,” 2014.

[6] IRENA, *Renewable Power Generation Costs in 2019*. 2019.

[7] Lazard, “Lazard’s Levelized Cost of Energy v. 13.0,” *Lazard.com*, no. November, pp. 1–21, 2019.

[8] National Research Council, N. R. Council, and National Research Council, *The National Academies Summit on America’s Energy Future: Summary of a Meeting*. Washington, DC: The National Academies Press, 2008.

[9] “Example of daily load profile for solar PV production relative to electricity demand in 2050 – Charts – Data & Statistics - IEA.” [Online]. Available: https://www.iea.org/data-and-statistics/charts/example-of-daily-load-profile-for-solar-pv-production-relative-to-electricity-demand-in-2050. [Accessed: 09-Jul-2020].

[10] S. Rehman, L. M. Al-Hadhrami, and M. M. Alam, “Pumped hydro energy storage system: A technological review,” *Renewable and Sustainable Energy Reviews*, vol. 44. Elsevier Ltd, pp. 586–598, 01-Apr-2015.

[11] T. M. Gü, “Review of electrical energy storage technologies, materials and systems: challenges and prospects for large-scale grid storage,” *2696 | Energy Environ. Sci*, vol. 11, p. 2696, 2018.

[12] H. Chen, G. Cong, and Y. C. Lu, “Recent progress in organic redox flow batteries: Active materials, electrolytes and membranes,” *J. Energy Chem.*, vol. 27, no. 5, pp. 1304–1325, Sep. 2018.

[13] A. Z. Weber, M. M. Mench, J. P. Meyers, P. N. Ross, J. T. Gostick, and Q. Liu, “Redox flow batteries: A review,” *J. Appl. Electrochem.*, vol. 41, no. 10, pp. 1137–1164, 2011.

[14] P. Alotto, M. Guarnieri, and F. Moro, “Redox flow batteries for the storage of renewable energy: A review,” *Renew. Sustain. Energy Rev.*, vol. 29, pp. 325–335, 2014.

[15] K. J. Kim, M. S. Park, Y. J. Kim, J. H. Kim, S. X. Dou, and M. Skyllas-Kazacos, “A technology review of electrodes and reaction mechanisms in vanadium redox flow batteries,” *J. Mater. Chem. A*, vol. 3, no. 33, pp. 16913–16933, 2015.

[16] E. Sum and M. Skyllas-Kazacos, “A study of the V(II)/V(III) redox couple for redox flow cell applications,” *J. Power Sources*, vol. 15, no. 2–3, pp. 179–190, Jun. 1985.

[17] K. T. Cho, P. Ridgway, A. Z. Weber, S. Haussener, V. Battaglia, and V. Srinivasan, “High Performance Hydrogen/Bromine Redox Flow Battery for Grid-Scale Energy Storage,” *J. Electrochem. Soc.*, vol. 159, no. 11, pp. A1806–A1815, 2012.

[18] M. Li, H. Su, Q. Qiu, G. Zhao, Y. Sun, and W. Song, “A Quaternized Polysulfone Membrane for Zinc-Bromine Redox Flow Battery,” 2014.

[19] W. Wang *et al.*, “A new redox flow battery using Fe/V redox couples in chloride supporting electrolyte.”

[20] J. O. Bockris and A. K. N. Reddy, *Modern Electrochemistry*. Springer US, 1970.

[21] C. Zhang *et al.*, “Progress and prospects of next-generation redox flow batteries,” *Energy Storage Mater.*, vol. 15, no. March, pp. 324–350, 2018.

[22] W. Wang, Q. Luo, B. Li, X. Wei, L. Li, and Z. Yang, “Recent progress in redox flow battery research and development,” *Adv. Funct. Mater.*, vol. 23, no. 8, pp. 970–986, 2013.

[23] R. Chen, S. Kim, and Z. Chang, “Redox Flow Batteries: Fundamentals and Applications,” in *Redox - Principles and Advanced Applications*, InTech, 2017.

[24] M. R. Mohamed, P. K. Leung, and M. H. Sulaiman, “Performance characterization of a vanadium redox flow battery at different operating parameters under a standardized test-

bed system,” *Appl. Energy*, vol. 137, pp. 402–412, Jan. 2015.

[25] P. Han *et al.*, “Graphene oxide nanoplatelets as excellent electrochemical active materials for VO2+/VO2+ and V2+/V3+ redox couples for a vanadium redox flow battery,” *Carbon N. Y.*, vol. 49, no. 2, pp. 693–700, Feb. 2011.

[26] Y. Shao *et al.*, “Nitrogen-doped mesoporous carbon for energy storage in vanadium redox flow batteries,” *J. Power Sources*, vol. 195, no. 13, pp. 4375–4379, Jul. 2010.

[27] K. V. Greco, A. Forner-Cuenca, A. Mularczyk, J. Eller, and F. R. Brushett, “Elucidating the Nuanced Effects of Thermal Pretreatment on Carbon Paper Electrodes for Vanadium Redox Flow Batteries,” *ACS Appl. Mater. Interfaces*, vol. 10, no. 51, pp. 44430–44442, 2018.

[28] L. Wei, T. S. Zhao, L. Zeng, X. L. Zhou, and Y. K. Zeng, “Copper nanoparticle-deposited graphite felt electrodes for all vanadium redox flow batteries,” *Appl. Energy*, vol. 180, pp. 386–391, 2016.

[29] L. F. Arenas, C. Ponce de León, and F. C. Walsh, “Three-dimensional porous metal electrodes: Fabrication, characterisation and use,” *Curr. Opin. Electrochem.*, vol. 16, pp. 1–9, 2019.

[30] H. Yu *et al.*, “Prompt Electrodeposition of Ni Nanodots on Ni Foam to Construct a High-Performance Water-Splitting Electrode: Efficient, Scalable, and Recyclable,” *Nano-Micro Lett.*, vol. 11, no. 1, 2019.

[31] A. Forner-Cuenca, E. E. Penn, A. M. Oliveira, and F. R. Brushett, “Exploring the Role of Electrode Microstructure on the Performance of Non-Aqueous Redox Flow Batteries,” *J. Electrochem. Soc.*, vol. 166, no. 10, pp. A2230–A2241, 2019.

[32] A. J. Bard, L. R. Faulkner, and J. Wiley, “ELECTROCHEMICAL METHODS Fundamentals and Applications,” 2001.

[33] R. Holze, *Experimental Electrochemistry*. Wiley-VCH, 2009.

[34] T. F. Fuller and J. N. Harb, “Electrochemical Engineering,” 2018.

[35] D. Sobha Jayakrishnan, “Electrodeposition: the versatile technique for nanomaterials,” in *Corrosion Protection and Control Using Nanomaterials*, Elsevier, 2012, pp. 86–125.

[36] J. O. (John O. . Bockris, 1923-, and G. A. Razumney, “Fundamental aspects of

electrocrystallization." Plenum Press, 1967.

[37] M. Haile Mamme, C. Köhn, J. Deconinck, and J. Ustarroz, "Numerical insights into the early stages of nanoscale electrodeposition: nanocluster surface diffusion and aggregative growth †," vol. 10, p. 7194, 2018.

[38] E. (Evgeni) Budevski, G. Staikov, and W. J. Lorenz, *Electrochemical phase formation and growth : an introduction to the initial stages of metal deposition*. VCH, 1996.

[39] A. Ray, "Electrodeposition of Thin Films for Low-cost Solar Cells," in *Electroplating of Nanostructures*, InTech, 2015.

[40] J. H. Van Der Merwe, "Crystal interfaces. Part II. Finite overgrowths," *J. Appl. Phys.*, vol. 34, no. 1, pp. 123–127, Jan. 1963.

[41] J. H. van der Merwe, "Structure of epitaxial crystal interfaces," *Surf. Sci.*, vol. 31, no. C, pp. 198–228, Jun. 1972.

[42] G. Abadias, L. Simonot, J. J. Colin, A. Michel, S. Camelio, and D. Babonneau, "Volmer-Weber growth stages of polycrystalline metal films probed by in situ and real-time optical diagnostics," *Appl. Phys. Lett.*, vol. 107, no. 18, p. 183105, Nov. 2015.

[43] Y. Wang, W. Chen, B. Wang, and Y. Zheng, "Ultrathin ferroelectric films: Growth, characterization, physics and applications," *Materials*, vol. 6, no. 9. MDPI AG, pp. 6377–6485, 2014.

[44] H. Brune, "Growth Modes," *Encycl. Mater. Sci. Technol.*, pp. 3683–3692, Jan. 2001.

[45] J. W. Dini and D. D. Snyder, "Electrodeposition of Copper," *Mod. Electroplat. Fifth Ed.*, pp. 33–78, 2011.

[46] N. C. Hoyt, K. L. Hawthorne, R. F. Savinell, and J. S. Wainright, "Plating Utilization of Carbon Felt in a Hybrid Flow Battery," *J. Electrochem. Soc.*, vol. 163, no. 1, pp. A5041–A5048, 2016.

[47] K. Nielsch, F. Müller, A. P. Li, and U. Gösele, "Uniform nickel deposition into ordered alumina pores by pulsed electrodeposition," *Adv. Mater.*, vol. 12, no. 8, pp. 582–586, 2000.

[48] D. L. Grimmett, M. Schwartz, and K. Nobe, "Pulsed Electrodeposition of Iron-Nickel Alloys," *J. Electrochem. Soc.*, vol. 137, no. 11, pp. 3414–3418, Nov. 1990.

[49] C. C. Yang and H. Y. Cheh, “Pulsed Electrodeposition of Copper/Nickel Multilayers on a Rotating Disk Electrode I. Galvanostatic Deposition,” *J. Electrochem. Soc.*, vol. 142, no. 9, pp. 3034–3040, 1995.

[50] D. E. Simpson, C. A. Johnson, and D. Roy, “Pulsed galvanostatic electrodeposition of copper on cobalt using a pH-neutral plating bath and electroless seeds,” *J. Electrochem. Soc.*, vol. 166, no. 1, pp. D3142–D3154, 2019.

[51] M. Zhou, N. Myung, X. Chen, and K. Rajeshwar, “Electrochemical deposition and stripping of copper, nickel and copper nickel alloy thin films at a polycrystalline gold surface: a combined voltammetry-coulometry-electrochemical quartz crystal microgravimetry study,” *J. Electroanal. Chem.*, vol. 398, no. 1–2, pp. 5–12, 1995.

[52] D. Grujicic and B. Pesic, “Electrodeposition of copper: the nucleation mechanisms.”

[53] V. A. Isaev, O. V Grishenkova, and Y. P. Zaykov, “Theory of cyclic voltammetry for electrochemical nucleation and growth.”

[54] T. I. Quickenden and X. Jiang, “The diffusion coefficient of copper sulphate in aqueous solution,” *Electrochim. Acta*, vol. 29, no. 6, pp. 693–700, 1984.

[55] E. McCafferty and E. McCafferty, “Thermodynamics of Corrosion: Pourbaix Diagrams,” in *Introduction to Corrosion Science*, Springer New York, 2010, pp. 95–117.

[56] L. Guo and P. C. Searson, “On the influence of the nucleation overpotential on island growth in electrodeposition,” *Electrochim. Acta*, vol. 55, no. 13, pp. 4086–4091, May 2010.

[57] G. A. Di Bari, “Electrodeposition of Nickel,” *Mod. Electroplat. Fifth Ed.*, pp. 79–114, 2011.

[58] I. Rose and C. Whittington, “Nickel plating handbook,” 2014.

[59] Y. Tsuru, M. Nomura, and F. R. Foulkes, “Effects of boric acid on hydrogen evolution and internal stress in films deposited from a nickel sulfamate bath,” *J. Appl. Electrochem.*, vol. 32, no. 6, pp. 629–634, 2002.

[60] Z. zhong Zuo, X. rong Zhou, and C. Zuo, “On the role of boric acid in the copper-tin alloy bath,” *Wuhan Univ. J. Nat. Sci.*, vol. 4, no. 2, pp. 211–215, 1999.

[61] E. Dávalos, R. López, H. Ruiz, A. Méndez, R. Antaño-López, and G. Trejo, “Study of the role of boric acid during the electrochemical deposition of Ni in a sulfamate bath,” *Int. J. Electrochem. Sci.*, vol. 8, no. 7, pp. 9785–9800, 2013.

[62] Z. Rao, S. J. Hearne, and E. Chason, “The Effects of Plating Current, Grain Size, and Electrolyte on Stress Evolution in Electrodeposited Ni,” *J. Electrochem. Soc.*, vol. 166, no. 1, pp. D3212–D3218, 2019.

[63] R. M. Smith, “Recent developments in the electrodeposition of nickel and some nickel-based alloys,” *Rev. Appl. Electrochem. Number*, vol. 63.

[64] W. Xu *et al.*, “Electrodeposited NiCu bimetal on carbon paper as stable non-noble anode for efficient electrooxidation of ammonia,” *Appl. Catal. B Environ.*, vol. 237, pp. 1101–1109, 2018.

[65] M. Moharana and A. Mallik, “Nickel electrocrystallization in different electrolytes: An in-process and post synthesis analysis,” *Electrochim. Acta*, vol. 98, pp. 1–10, 2013.

[66] J. X. Kang, W. Z. Zhao, and G. F. Zhang, “Influence of electrodeposition parameters on the deposition rate and microhardness of nanocrystalline Ni coatings,” *Surf. Coatings Technol.*, vol. 203, no. 13, pp. 1815–1818, 2009.

[67] K. R. Mamaghani and S. M. Naghib, “The effect of stirring rate on electrodeposition of nanocrystalline nickel coatings and their corrosion behaviors and mechanical characteristics,” *Int. J. Electrochem. Sci.*, vol. 12, no. 6, pp. 5023–5035, 2017.

[68] H. Ni *et al.*, “Fabrication and characterization of nanocrystalline nickel with a grain size gradient by direct current electrodeposition,” *Int. J. Electrochem. Sci.*, vol. 14, no. 9, pp. 8429–8438, 2019.

[69] Y. F. Wang, C. X. Huang, X. T. Fang, H. W. Höppel, M. Göken, and Y. T. Zhu, “Hetero-deformation induced (HDI) hardening does not increase linearly with strain gradient,” *Scr. Mater.*, vol. 174, pp. 19–23, 2020.

[70] M. Yang, Y. Pan, F. Yuan, Y. Zhu, and X. Wu, “Back stress strengthening and strain hardening in gradient structure,” *Mater. Res. Lett.*, vol. 4, no. 3, pp. 145–151, Jul. 2016.

[71] K. D. Song, K. B. Kim, S. H. Han, and H. K. Lee, “A study on effect of hydrogen reduction reaction on the initial stage of Ni electrodeposition using EQCM,” *Electrochem. commun.*, vol. 5, no. 6, pp. 460–466, 2003.

[72] K. Neuróhr, L. Pogány, B. G. Tóth, Révész, I. Bakonyi, and L. Péter, “Electrodeposition of Ni from various non-aqueous media: The case of alcoholic solutions,” *J. Electrochem. Soc.*, vol. 162, no. 7, pp. D256–D264, 2015.

[73] J. Wojciechowski, M. Baraniak, J. Pernak, and G. Lota, “Nickel coatings electrodeposited from watts type baths containing quaternary ammonium sulphate salts,” *Int. J. Electrochem. Sci.*, vol. 12, no. 4, pp. 3350–3360, 2017.

[74] A. P. Abbott, A. Ballantyne, R. C. Harris, J. A. Juma, and K. S. Ryder, “A Comparative Study of Nickel Electrodeposition Using Deep Eutectic Solvents and Aqueous Solutions,” *Electrochim. Acta*, vol. 176, pp. 718–726, 2015.

[75] A. S. C. Urcezino, L. P. M. Dos Santos, P. N. S. Casciano, A. N. Correia, and P. De Lima-Neto, “Electrodeposition study of Ni coatings on copper from choline chloride-based deep eutectic solvents,” *J. Braz. Chem. Soc.*, vol. 28, no. 7, pp. 1193–1203, 2017.

[76] Y. L. Zhu, Y. Kozuma, Y. Katayama, and T. Miura, “Electrochemical behavior of Ni(II)/Ni in a hydrophobic amide-type room-temperature ionic liquid,” *Electrochim. Acta*, vol. 54, no. 28, pp. 7502–7506, 2009.

[77] B. Meenatchi, V. Renuga, and A. Manikandan, “Electrodeposition of Nickel on Glassy Carbon Electrode from Protic Ionic Liquids with Imidazolium Cation,” *J. Inorg. Organomet. Polym. Mater.*, vol. 26, no. 2, pp. 423–430, 2016.

[78] A. P. Abbott and K. J. McKenzie, “Application of ionic liquids to the electrodeposition of metals,” *Phys. Chem. Chem. Phys.*, vol. 8, no. 37, pp. 4265–4279, 2006.

[79] F. Liu, Y. Deng, X. Han, W. Hu, and C. Zhong, “Electrodeposition of metals and alloys from ionic liquids,” *J. Alloys Compd.*, vol. 654, pp. 163–170, 2016.

[80] Y. L. Zhu, Y. Katayama, and T. Miura, “Effects of acetonitrile on electrodeposition of Ni from a hydrophobic ionic liquid,” *Electrochim. Acta*, vol. 55, no. 28, pp. 9019–9023, Dec. 2010.

[81] L. Sun, C. L. Chien, and P. C. Searson, “Fabrication of nanoporous nickel by electrochemical dealloying,” *Chem. Mater.*, vol. 16, no. 16, pp. 3125–3129, 2004.

[82] R. Y. Ying, “Electrodeposition of Copper-Nickel Alloys from Citrate Solutions on a Rotating Disk Electrode,” *J. Electrochem. Soc.*, vol. 135, no. 12, p. 2957, 1988.

[83] "SEM Scanning Electron Microscope A To Z."

[84] D. Goranova, G. Avdeev, and R. Rashkov, "Electrodeposition and characterization of Ni-Cu alloys," *Surf. Coatings Technol.*, vol. 240, pp. 204–210, Feb. 2014.

[85] R. A. Butera and D. H. Waldeck, "X-ray diffraction investigation of alloys," *J. Chem. Educ.*, vol. 74, no. 1, pp. 115–119, 1997.

Symbols, Constants, Indices and Abbreviations

Symbols

Symbol	Description	Units
a	Activity	[-]
A	Area	[cm^2]
C_{spec}	Specific capacitance	[$F\ cm^{-2}$]
E	Potential	[V]
ECSA	Electrochemically active surface area	[$m^2\ g^{-1}$]
EDLC	Electrochemical double layer capacitance	[F]
I or ι	Current	[A]
j	Current density	[$A\ cm^{-2}$]
m	Mass	[g]
m_e	Electrode mass	[g]
Q	Total electric charge	[A s]
Q_r	Reaction quotient of cell reaction	[-]
T	Temperature	[K]
t	Time	[s]
U	Voltage	[V]
V	Volume	[L]
z	Number of electrons in (half-)reaction	[-]
ΔG	Gibbs free energy	[$J\ mol^{-1}$]
η	Overpotential	[V]
ι_{EDLC}	Average capacitive current	[A]
ρ	Roughness factor	[-]

Constants

Symbol	Description	Value	Units
F	Faraday's constant	96485	[$A\ s\ mol^{-1}$]
R	Universal gas constant	8.314	[$J\ K^{-1}\ mol^{-1}$]
κ	Shape factor	~1	[-]

Indices

Symbol	**Description**
$(\,)_a$	Anodic
$(\,)_{act}$	Activation
$(\,)_c$	Cathodic
$(\,)_{geo}$	Geometrical
$(\,)_i$	Initial
$(\,)_{mt}$	Mass transfer
$(\,)_{off}$	Off
$(\,)_{ohmic}$	Ohmic
$(\,)_{on}$	On
$(\,)_{Ox}$	Oxidation
$(\,)_{real}$	Real
$(\,)_{Red}$	Reduction

Abbreviations

Abbreviation	**Description**
2D	Two-dimensional
3D	Three-dimensional
ac	Alternating current
CE	Current/coulombic efficiency
cps	Counts per second
CV	Cyclic voltammetry
dc	Direct current
ED	Electrodeposition
EDS/EDX	Energy dispersive X-ray spectroscopy
EE	Energy efficiency
EQCM	Electrochemical quartz crystal microbalance
fcc	Face-centered cubic
FIB-SEM	Focused ion beam scanning electron microscope
HER	Hydrogen evolution reaction
IEM	Ion exchange membrane

LSV	Linear sweep voltammetry
OCV	Open circuit voltage
OER	Oxygen evolution reaction
P.C.	Probe current
PED	Pulsed electrochemical deposition
RFB	Redox flow battery
SEM	Scanning electron microscope
STM	Scanning tunneling microscopy
VRFB	Vanadium redox flow battery
XPS	X-ray photoelectron spectroscopy
XRD	X-ray diffraction